LIVERPOOL JOHN MOORES UNIVERSITY

LJMU Research Online

Huang, H, Liu, Q, Iglesias, G and Li, C

Advanced multi-physics modeling of floating offshore wind turbines for aerodynamic design and load management

https://researchonline.ljmu.ac.uk/id/eprint/27322/

Article

Citation (please note it is advisable to refer to the publisher's version if you intend to cite from this work)

Huang, H, Liu, Q ORCID logoORCID: https://orcid.org/0009-0001-1925-652X, Iglesias, G ORCID logoORCID: https://orcid.org/0000-0003-2719-1663 and Li, C (2025) Advanced multi-physics modeling of floating offshore wind turbines for aerodynamic design and load management. Energy Conversion

LJMU has developed **LJMU Research Online** for users to access the research output of the University more effectively. Copyright © and Moral Rights for the papers on this site are retained by the individual authors and/or other copyright owners. Users may download and/or print one copy of any article(s) in LJMU Research Online to facilitate their private study or for non-commercial research. You may not engage in further distribution of the material or use it for any profit-making activities or any commercial gain.

The version presented here may differ from the published version or from the version of the record. Please see the repository URL above for details on accessing the published version and note that access may require a subscription.

For more information please contact researchonline@ljmu.ac.uk

http://researchonline.ljmu.ac.uk/

Energy Conversion and Management 346 (2025) 120437

Contents lists available at ScienceDirect

Energy Conversion and Management

journal homepage: www.elsevier.com/locate/enconman

Advanced multi-physics modeling of floating offshore wind turbines for aerodynamic design and load management

Haoda Huang [a], Qingsong Liu [b,*], Gregorio Iglesias [c,d], Chun Li [a]

[a] School of Energy and Power Engineering, University of Shanghai for Science and Technology, Shanghai 200093, China
[b] School of Engineering, University of Liverpool, The Quadrangle, Brownlow Hill L69 3GH, United Kingdom
[c] School of Engineering and Architecture, University College Cork, College Rd., Cork T12 K8AF, Ireland
[d] School of Engineering, Computing and Mathematics, University of Plymouth, Drake Circus, Plymouth PL4 8AA, United Kingdom

ARTICLE INFO

Keywords:
Floating offshore wind turbine
Computational fluid dynamics
Finite element analysis
Fully coupled dynamics
Fluid-structure interaction

ABSTRACT

Floating offshore wind turbines (FOWTs) offer distinct advantages for improving the competitiveness of offshore wind energy. However, their operation involves complex dynamics characterized by multiple sources of loading, considerable temporal variability, and high nonlinearity. Understanding the multi-physics coupling mechanisms and subsystem interactions governing the behavior of FOWTs is essential for enhancing operational safety, increasing power output, and promoting commercial deployment. To address these challenges, this study develops a high-fidelity, fully coupled aero-elastic-hydro-mooring framework by integrating computational fluid dynamics (CFD) and the finite element method (FEM). The NREL 5 MW horizontal-axis wind turbine (HAWT) mounted on a semi-submersible platform is used as an exemplar to investigate its nonlinear dynamic responses under combined wind and wave loading. The results show that the platform's six-degree-of-freedom motion leads to continuous changes in the rotor inflow conditions, resulting in a 6.84 % reduction in the average power coefficient compared with its bottom-fixed counterpart, and producing a noticeable increase in power fluctuations. Nevertheless, the wake behind the FOWT exhibits higher turbulence intensity and a faster rate of dissipation. The two-way fluid–structure interaction analysis indicates that the blades undergo flapwise elastic deformation, particularly from the mid-span to the tip, which alters the angle of attack and induces continuous vortex shedding along the trailing edges. The structural stress distribution highlights significant stress concentration at the tower base, the bottom of the main column, and the connections between the braces and the platform. Although blade stress remains relatively low overall, higher stresses are observed near the blade root transition and at the shear web connections. In addition, the contact opening analysis between the mooring lines and the seabed shows that the windward mooring line periodically separates from and recontacts the seabed due to the surge motion of the platform, resulting in varying contact pressure distributions and large fluctuations in the mooring tension.

1. Introduction

Wind energy has emerged as a focal point in the global energy transition due to its environmental friendliness and sustainability [1]. Particularly, the exploitation of high-quality offshore wind resources has become a crucial pathway for achieving the global net-zero carbon emission targets [2], not least thanks to their higher energy density and potential for large-scale utilization [3]. As of early 2025, the total installed capacity of offshore wind power worldwide has reached 83.2 GW, with installations from the past five years accounting for 66.81 % of the total [4].

At present, offshore wind technology relies predominantly on bottom-fixed foundations, which present two fundamental limitations [5]: the restriction to shallow continental shelf regions, excluding deep-water offshore areas with greater wind energy potential, such as the Celtic Sea; and the requirement for on-site assembly of wind turbines, which introduces significant complexities and, therefore, costs in the installation and commissioning processes. Furthermore, constrained by navigational space allocation and environmental impact considerations, most suitable shallow-water areas for bottom-fixed turbine deployment worldwide have approached saturation – the North Sea being the most typical example [6]. Consequently, wind energy development must

* Corresponding author.
E-mail address: Qingsong.liu@liverpool.ac.uk (Q. Liu).

https://doi.org/10.1016/j.enconman.2025.120437
Received 16 July 2025; Received in revised form 13 August 2025; Accepted 25 August 2025
Available online 30 August 2025
0196-8904/© 2025 The Author(s). Published by Elsevier Ltd. This is an open access article under the CC BY license (http://creativecommons.org/licenses/by/4.0/).

transition to deeper offshore regions. In this context, floating offshore wind turbines (FOWTs) have been technically validated as a viable alternative to bottom-fixed systems, leveraging advantages in modular floating structure design and water depth adaptability [7].

1.1. Multi-physics field coupling challenges

The FOWT system exhibits multiple sources of loading, strongly time-varying, and nonlinear characteristics. Under the combined excitation of wind, waves, and currents, its subsystems (platform, rotor, tower, nacelle, and mooring) interact with one another, forming a dynamic closed-loop coupling: the platform six-degree-of-freedom (6-DOF) motion → tower motion → change of rotor inflow condition → aerodynamic load variation → platform motion feedback. This persistent interaction maintains the system in a state of force imbalance and unsteady motion [8,9], as shown in Fig. 1. Furthermore, the in-service environment of FOWTs is dominated by complex turbulent flows with spatiotemporal stochasticity [10]. Asymmetric inflow conditions (e.g., turbulent winds and nonlinear waves) induce highly non-uniform aerodynamic load distributions across the rotor swept area, increasing blade root bending moments as well as tower overturning moments, which significantly reduce aerodynamic efficiency and contribute to structural fatigue [11]. The trend toward large-scale, deep-sea FOWTs [12] will likely exacerbate the issues caused by these multi-physics field effects, which will primarily manifest as increased aeroelastic instability (flutter) due to bending-torsion coupling and structural resonance risks induced by low-frequency turbulence excitation [13,14]. To accelerate the commercialization of FOWTs and reduce the levelized cost of energy (LCOE), elucidating these coupled multi-physical interaction mechanisms is imperative. This will provide foundational insights for the optimization of FOWT design through load mitigation and stability enhancement.

Because of the complex environmental loading conditions in deep sea regions and high costs, conducting mid-scale experimental testing for FOWT systems remains challenging [15]. Although scaled tank testing can validate design concepts and simulation accuracy, the scaling effects prevent the simultaneous satisfaction of both Reynolds and Froude similarity criteria. When considering the Froude-scaled conditions, the aerodynamic thrust of scaled models is typically underestimated compared to full-scale predictions [16,17]. Therefore, revealing cross-scale and multi-physics coupling effects in FOWTs through high-fidelity numerical modeling is critical, as such models serve as an important complement to experimental validation by resolving the scaling law conflicts inherent in physical testing.

1.2. Overview of fully coupled method for FOWTs

Presently, the fully coupled modeling of FOWTs relies primarily on mid-fidelity numerical models, with widely used tools including OpenFAST, HAWC2, and Bladed [18]. These tools generally employ modular partitioned modeling frameworks to achieve multi-physics coupled dynamic simulations of FOWTs. By incorporating simplified models based on engineering experience, mid-fidelity numerical models exhibit significant advantages regarding computational efficiency and parametric sensitivity analysis capabilities [19]. In recent years, mid-fidelity fully coupled modeling for FOWTs has been further extended with co-simulation frameworks through interface coupling that combine the strengths of different tools. However, despite their enhanced precision, these models still cannot fully capture the multi-physics coupled dynamic behavior of FOWTs under complex sea conditions. Table 1 summarizes the current primary mid-fidelity fully coupled modeling tools and solution methods for FOWTs.

In the design and optimization of FOWTs, the need to thoroughly understand and characterize their complex nonlinear coupled dynamics has driven the rapid development of high-fidelity numerical models based on computational fluid dynamics (CFD) [26]. By numerically solving the Navier-Stokes equations, which account for viscous effects, the CFD approach can effectively address complex flows, extreme sea

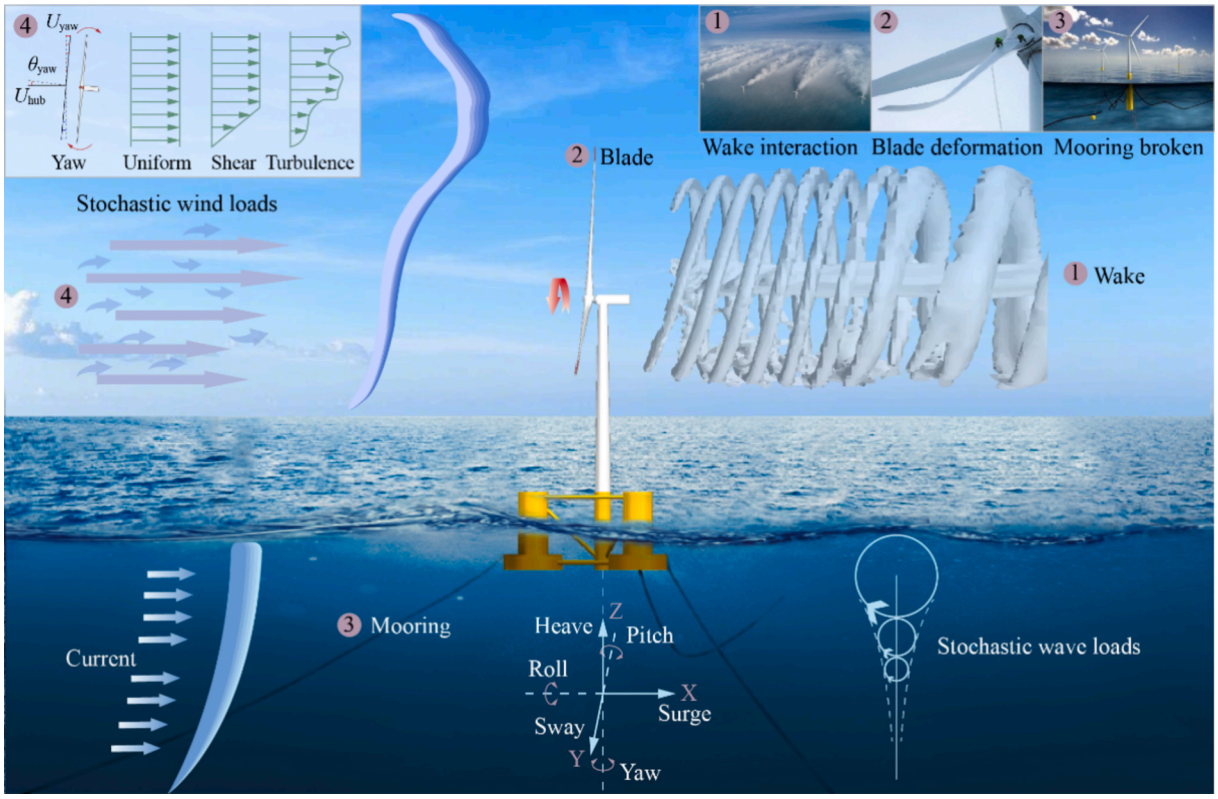

Fig. 1. The complex multi-physics coupling dynamic behavior of FOWTs.

Table 1
Primary mid-fidelity fully coupled numerical modeling technologies for FOWTs.

Coupling tools	Aerodynamics	Hydrodynamics	Structural dynamics	Mooring dynamics	Blade modeling
FAST-AQWA [20]	BEMT + DWM	LWT + PFT	MBD	DM	BE
OrcaWave-OrcaFlex [21]	BEMT	LWT + PFT	MBD	DM	RB
AeroDyn-SIMPACK [22]	BEMT	LWT + PFT + ME	MBD + MA	QSM	BE
OrcaFlex-Hydrostar [23]	VLM	LWT + PFT	MBD	DM	RB
OpenFAST-WEC-sim [24]	BEMT + DWM	LWT + PFT	MBD	DM	BE
HYDRAN-XR [25]	BEMT	LWT + PFT	MBD + FEM	QSM	SE

BEMT: blade element momentum theory; DWM: dynamic wake model; VLM: vortex lattice method; LWT: linear wave theory; PFT: potential flow theory; ME: Morison equation; MBD: multi-body dynamics; MA: modal analysis; FEM: finite element method; DM: dynamic model; QSM: quasi- static model; RB: rigid body; BE: beam element; SE: shell element.

conditions, and nonlinear challenges specific to FOWTs [27]. Current CFD studies on FOWTs primarily include uncoupled and fully coupled analyses. The former employs predefined platform motion functions combined with overset mesh technology to simulate single/multi-DOF reciprocating motions of FOWTs. Notably, platform and mooring modeling are often omitted during simulations to reduce computational costs.

Sun et al. [28] established a full-scale CFD model of the FOWT to investigate the effects of the tower shadow and platform surge motion on the aerodynamic performance of a downwind FOWT. Their results revealed that, under identical surge motion conditions, the average rotor thrust and torque of the downwind FOWT were comparable to those of its upwind counterpart. The tower shadow effect induced periodic abrupt drops in rotor thrust and torque, the drop magnitude being significantly higher for the downwind configuration. The surge motion amplified or attenuated these drops by altering instantaneous relative wind speeds. Guo et al. [29] imposed combined pitch-surge platform motions and examined the influence of motion frequency and initial phase differences on FOWT aerodynamic performance. Their findings demonstrated that such combined motions increased operational instability. In-phase and coupling of multiple frequencies led to pronounced fluctuations in power and thrust, with the dominant frequency determined by the lower frequency component. Subsequently, Cai et al. [30] conducted an analysis from a distinct perspective on the aerodynamic mechanisms of the FOWT under coupled surge-pitch motions. Their study revealed that under in-phase coupled motions, the wind turbine undergoes dynamic stall and the vortex ring state (VRS). The dynamic stall resulted in continuous tip vortex shedding, exacerbating flow complexity behind the tower and nacelle. Additionally, the VRS-induced recirculation of tip and root vortices generated negative values of thrust and torque. To improve the CFD computational efficiency, the actuator line model (ALM) was developed as a volumetric force method to replace three-dimensional blades. In this model, rotating momentum source lines represent each blade, eliminating the need for high-resolution grids near the blade surface. Arabgolarcheh et al. [31] coupled ALM with the CFD to investigate the wake characteristics of the FOWTs under forced motion. They found that the platform movement significantly influences wake characteristics, with complex changes in wake vortices spacing during pitch motion. Subsequently, they further applied the CFD-ALM model to study the wake interactions of tandem FOWTs under varying pitch and surge motions of the upstream turbine. While discrete tip vortices generated by the upstream turbine blades did not affect the frequency characteristics of the downstream turbine loads, their evolution into ring-shaped wakes influenced by platform motion significantly increased the peak fluctuations [32]. These studies highlight that the decoupled CFD and CFD-ALM simulations can isolate specific DOFs and reduce model complexity, but they cannot capture real-time coupling mechanisms in realistic sea conditions, potentially underestimating strongly nonlinear loads.

To address this problem, recent studies have progressively developed fully coupled numerical models for FOWTs using CFD. Zhou et al. [33] performed a high-fidelity aero-hydrodynamic analysis of a 5 MW semi-submersible FOWT using CFD, investigating the impacts of wave types (e.g., focused waves, irregular waves) and wave steepness on its performance. Their results demonstrated that under identical wave spectra, focused and irregular waves significantly influenced hydrodynamic responses, with wave diffraction and substantial wave run-ups captured accurately by CFD. Subsequently, the same numerical framework was extended to examine the influence of turbulent and shear winds on the coupled dynamics of FOWTs. The study revealed that turbulent winds altered near-wake airflow distribution, increasing the standard deviation of power output, while thick shear wind layers induced localized power decreases. However, the turbulence frequency being far below the FOWT's natural frequency, its impact on platform and mooring dynamics remained limited [34]. Alkhabbaz et al. [35] established a coupled aero-hydro-mooring dynamic model for a 5 MW semi-submersible FOWT using CFD, with comprehensive validation against FAST and OrcaFlex. The CFD results indicated that the superposition of incoming wind and platform surge velocity markedly modified the apparent wind velocity perpendicular to the rotor plane, resulting in the periodic fluctuations of power output. Furthermore, surge motion accelerated wake velocity recovery compared to bottom-fixed turbines, offering insights for optimizing wake interference in offshore wind farms.

These studies confirm that CFD can effectively capture the nonlinear dynamic responses and complex vortex wake structures of the FOWTs. However, research so far has predominantly relied on 6-DOF rigid-body models or dynamic fluid-body interaction (DFBI) frameworks for platform motion and multi-body dynamics coupling, with mooring systems commonly simplified by a quasi-static model.

1.3. Research challenge and motivation

The mid-fidelity and high-fidelity numerical modeling methods discussed in Section 1.2 provide valuable guidance for developing fully coupled FOWT models and elucidating multi-physics coupling mechanisms. However, these approaches still exhibit limitations:

- Current aerodynamic analyses of FOWTs predominantly employ blade element momentum theory (BEMT). While BEMT achieves computational efficiency and maintains reasonable accuracy, its fundamental assumption of steady uniform flow inherently conflicts with the nonlinear dynamic characteristics of FOWTs, thereby failing to capture transient aerodynamic effects such as turbulent inflow [36]. Furthermore, the VRS effects induced by FOWT surge motion violate the momentum conservation principles underlying BEMT solutions [37].
- Compared to full CFD simulation, ALM offers higher computational efficiency and effectively resolves dynamic flow fields, which is suitable for large-scale simulations and the calculation of multiple operating conditions [38]. However, it lacks the accuracy for FOWT analysis, particularly in strong nonlinear conditions, where complex aerodynamic behavior like blade stall and flow separation are critical [39].
- Potential flow theory (PFT) simplifies hydrodynamic equations through velocity potential function solutions based on inviscid,

irrotational, and incompressible assumptions [40]. However, the hydrodynamics of FOWTs involve complex coupling processes among waves, platforms, and mooring systems, featuring significant viscous effects, turbulent dissipation, and multiphase flow interactions. The neglect of fluid viscosity and vorticity in PFT prevents the accurate characterization of the hydrodynamic behavior of FOWTs.

- Quasi-static models (QSM), commonly used to model the mooring system, employ static equilibrium assumptions that disregard inertial and damping effects [41]. An accurate prediction of mooring tension is critical for structural safety assessment in FOWT systems. QSM may underestimate cumulative damage in mooring systems during long-term operation, potentially leading to conservative designs and safety risks.
- Most fully coupled FOWT simulations simplify blades as rigid bodies or beam elements. Such simplifications neglect flexible blade deformations or fail to address the anisotropic characteristics of composite laminated structures and geometric nonlinear responses, thereby limiting aeroelastic coupling analysis accuracy [42]. Particularly for modern large-scale FOWTs, the coupled flapwise-edgewise-torsional deformation problem becomes increasingly prominent, making precise prediction of blade aeroelastic effects crucial.

In conclusion, to systematically reveal the multi-physics coupled dynamic mechanisms of FOWTs to advance their technological commercialization, the development of a more precise and advanced numerical model is necessary.

1.4. Present work

This study develops a high-fidelity, fully coupled numerical model capable of comprehensively analyzing the aero-elastic-hydro-mooring dynamic behavior of the FOWT. A detailed description of the fluid–structure interaction (FSI) framework adopted is provided, including geometric modeling, material distribution, blade laminate scheme design, and parameter settings. Specifically, the CFD method is employed to account for fluid viscosity, air–water two-phase flow evolution, and the interactions with wake structures, while the finite element method (FEM) is used to analyze the nonlinear structural response and mooring dynamics of the FOWT. The main contributions are:

(1) The nonlinear response mechanisms of aerodynamic power and thrust in FOWTs are revealed, along with an in-depth analysis of the flapwise-edgewise-torsional coupling behavior of individual blades. The flow field visualizations further illustrate large-scale flow separation and vortex shedding within the rotor swept area of both FOWTs and bottom-fixed wind turbines, with comparative analysis of their wake evolution and velocity deficits.

(2) The dynamic response of the FOWT platform under the combined effects of wind-wave loads and mooring restoring forces and moments is clarified. The interaction between mooring tension response and the platform's 6-DOF motions is analyzed. Furthermore, a dynamic model is employed to account for frictional contact between the mooring and the seabed, and the mooring opening distance as well as the contact stress are investigated.

(3) The stress distribution characteristics of the FOWT tower, platform, blades, and internal shear webs are examined, with additional analysis focused on blade flapwise deformation. The underlying physical mechanisms of the blade aeroelastic response are elucidated through surface velocity fields, vorticity distributions, and streamline patterns.

The fully coupled numerical model developed in this study offers a valuable approach for accurately resolving the dynamic behavior of FOWTs under complex multi-physics coupling conditions and provides meaningful insights for future performance optimization and design improvements.

2. Model establishment

2.1. Full-scale model

This study investigates the DeepCwind semi-submersible platform from the OC4 Phase II project, equipped with an NREL 5 MW horizontal axis wind turbine (HAWT). The full-scale model of the 5 MW semi-submersible FOWT is illustrated in Fig. 2. During hub modeling, a blade root cone angle of 2.5 deg is preconfigured, with a predefined nacelle tilt angle of 5 deg at the nacelle interface. The HAWT blades are modeled with updated airfoil profiles [43]. The semi-submersible platform is characterized by an equilateral triangular configuration with 50 m side lengths, where three vertical columns are positioned at the triangular vertices and one central column is at the centroid. The height of the platform above the still water level (SWL) is 20 m, with its center of mass (COM) positioned 13.46 m below the SWL. In this study, to achieve smoother transitions at structural joints, minor angular adjustments to the diagonal braces are implemented, while all other geometric dimensions remain consistent with the design report. The detailed modeling specifications refer to the design report [44]. The operational parameters of the 5 MW FOWT are presented in Table 2.

2.2. Material distribution

2.2.1. 5 MW FOWT

The large-scale and deep-sea development of FOWTs necessitates blades with superior mechanical properties to withstand increasingly complex extreme loads, requiring rational structural design to balance weight and load-bearing capacity. This has driven the widespread application of composite materials in the layup design of large-scale wind turbine blades. The use of composite materials enhances blade performance, effectively reduces blade mass, and improves overall wind turbine efficiency and reliability. The 5 MW blade layup scheme adopted in this study references publicly available data from Sandia National Laboratories [45]. During the layup processes, the blade surface is typically divided into six chordwise regions based on the relative positions of shear webs within the blade, as shown in Fig. 3. The layup materials include gelcoat, biaxial/triaxial skins, foam, carbon fiber, and glass fiber reinforced polymer (GFRP). The layup sequence follows: (a) the entire 5 MW blade area uses triaxial skin as the substrate; (b) the main spar, positioned at the pitch center as the primary load-bearing structure, employs high-strength, low-density carbon fiber; (c) the leading edge region employs foam material as the core layer; (d) the trailing edge core layer incorporates foam supplemented with GFRP to enhance structural strength; (e) the web utilizes a sandwich core structure, with foam serving as the core layer and biaxial skin layers applied on both surfaces; (f) the blade root, being the critical load-bearing section, receives extra triaxial skin layers for strength enhancement; (g) a gelcoat layer coats the blade surface to prevent environmental degradation and reduce surface roughness. The composite layup sequence and number of laminate plies along the blade spanwise direction are shown in Table 3 and Fig. 4.

For the hub, nacelle, and tower, a steel structure with a density of 8,500 kg/m^3 is adopted. Since there are no design specifications for the hub and nacelle, their final masses are kept essentially consistent with Ref. [43] by adjusting the wall thickness. Unlike the fixed-foundation towers, the floating tower has a total height of 77.6 m, and its mass density decreases gradually with increasing height. This study divides the tower into 10 sections and maintains the mass consistency of each section with the Ref. [44] by modifying the wall thickness. The COM of the finalized tower CAE model is located 45.37 m above the SWL – a 4.54 % deviation from the design report value (43.4 m). The total mass of the 5 MW HAWT CAE model is 600,213 kg – a 0.086 % deviation with respect to the theoretical result (599,698 kg). This discrepancy arises because of the complete modeling of the blade tip section in this work, i.e., the additional mass results from considering the composite material

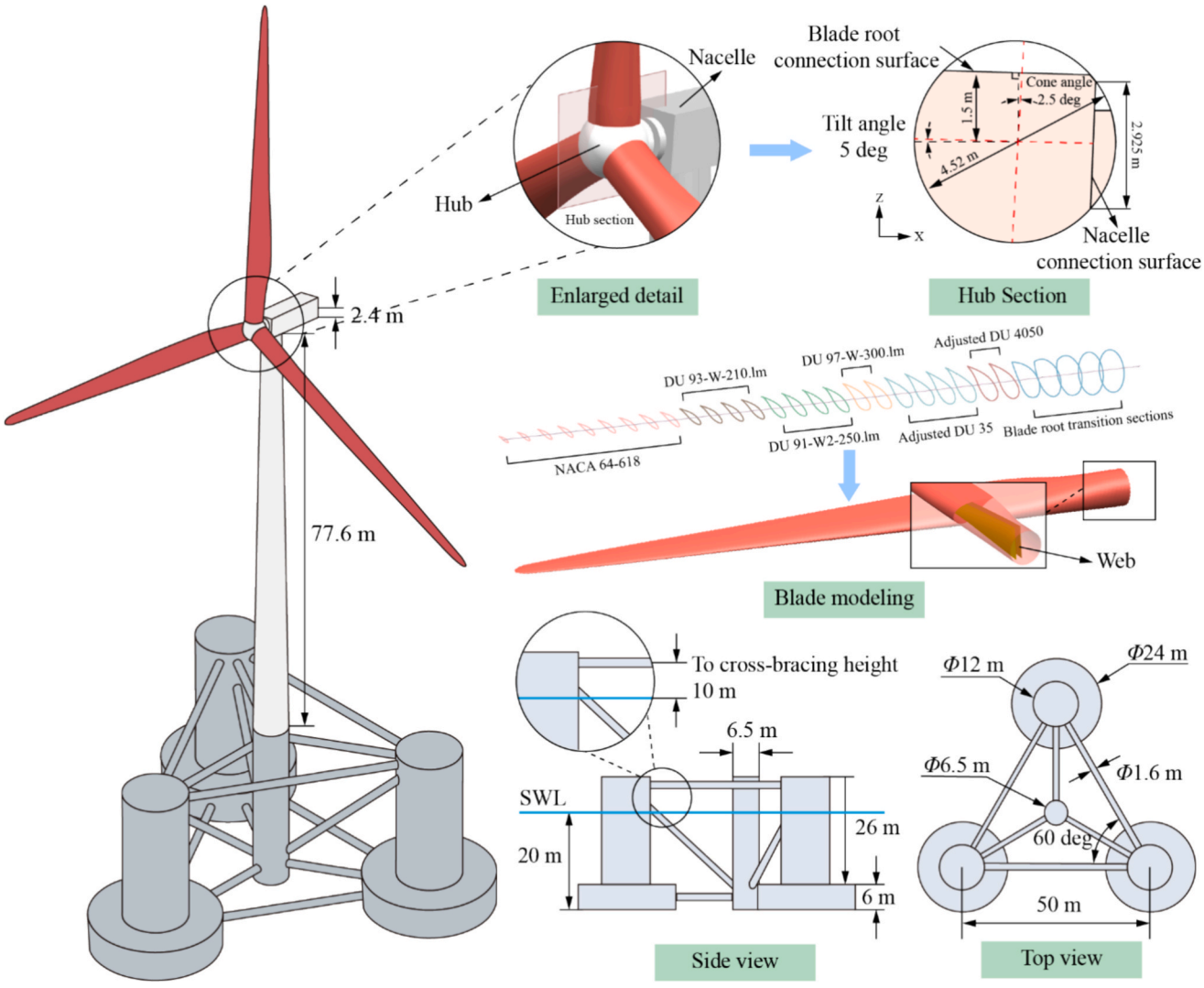

Fig. 2. Real-scale modeling of the 5 MW semi-submersible FOWT.

Table 2
Operational parameters of the 5 MW FOWT.

Parameters	Values
Rated wind speed	11.4 m·s^{-1}
Rated rotational speed	12.1 rpm
Hub overhang	5 m
Tilt angle and cone angle	5 deg, 2.5 deg
Height of hub	90 m
Height of tower	87.6 m
Hub and rotor diameters	3 m, 126 m

layup at the tip.

The OC4 semi-submersible platform employs steel structures with a density of 7,850 kg/m^3 and a Young's modulus of 2.1 × 10^{11} Pa. The wall thicknesses of the pontoons, main columns, and braces are 0.06 m, 0.03 m, and 0.0175 m, respectively, as shown in Fig. 5. To maintain platform stability, ballast water is filled in both the base and upper pontoons. Due to minor angular adjustments to the diagonal braces, the total platform mass (excluding ballast water) increases, necessitating corresponding adjustments to the ballast water heights in the upper and base pontoons in this study. Additionally, the ballast water is modeled as solid elements with a density of 1,025 kg/m^3 and subjected to tied constraints with the inner surfaces of the pontoons. The specific parameters of the platform CAE model are summarized in Table 4.

2.2.2. Mooring

The mooring system ensures safe and stable operation of the FOWT by providing restoring moments. In the semi-submersible FOWT configuration, mooring fairleads are mounted on three base pontoons, spaced 120 deg apart, and the contact interaction between the mooring line and the seabed is considered. The equivalent material properties of the mooring are summarized in Table 5.

2.3. Parameters definition

The tip-speed ratio λ_{tip}, a core parameter in the aerodynamic design of wind turbines, is defined as the ratio of the linear velocity at the blade tip to the incoming wind speed [46]:

$$\lambda_{tip} = \frac{\omega_{tip} \cdot R_r}{V_f} \tag{1}$$

where ω_{tip} is the rotor angular velocity, R_r is the rotor radius, and V_f is the undisturbed incoming wind velocity.

The thrust (T_b) and power (P_b) characterize the structural load-bearing characteristics and energy conversion efficiency of FOWT. The thrust represents the axial resultant force generated by wind loads acting on the turbine blades, while power denotes the mechanical energy extracted from the wind. Their definitions are given as [47,48]:

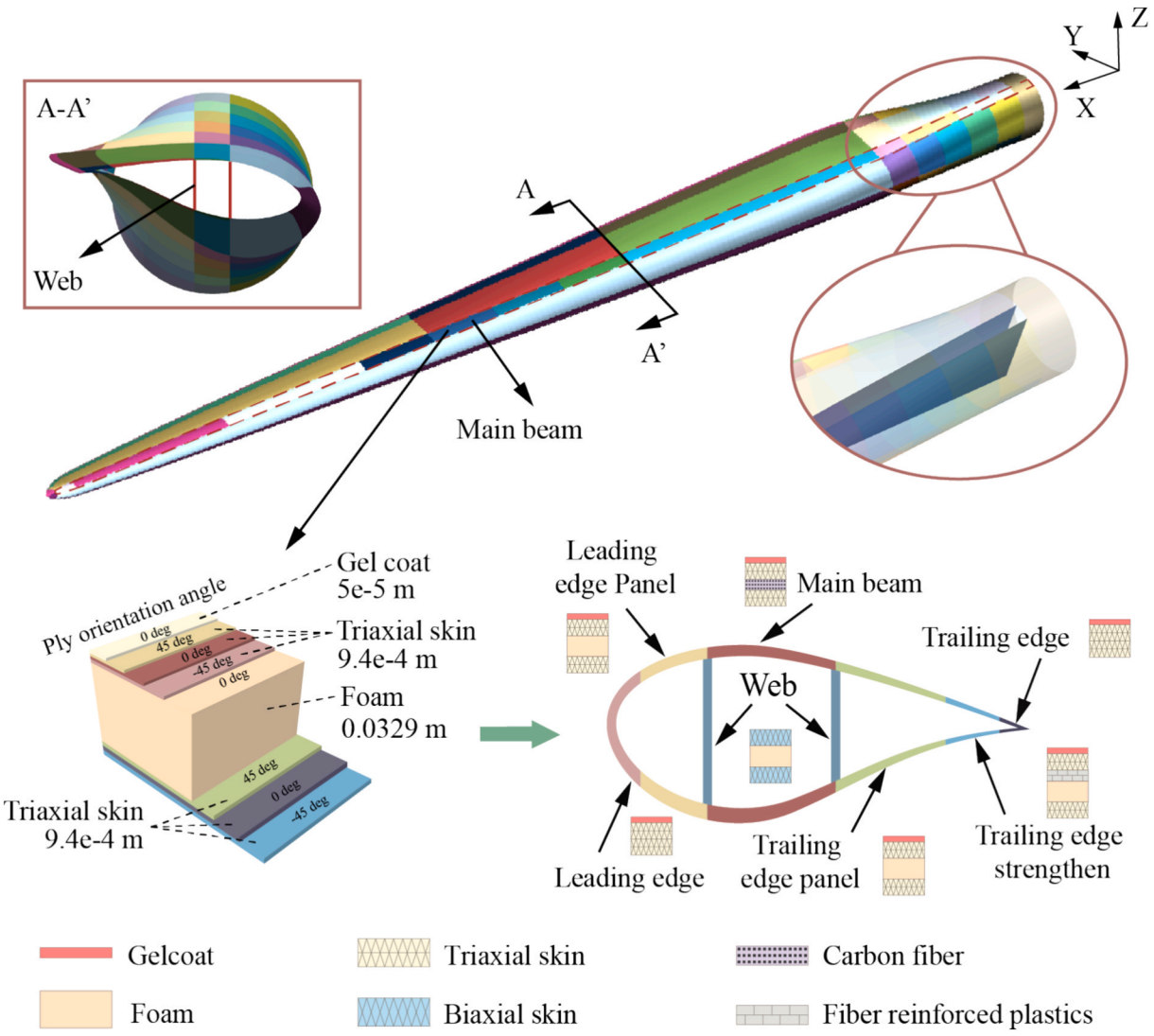

Fig. 3. 5 MW blade composite material distribution.

Table 3
Layup sequence of composite materials along the blade spanwise.

Chordwise segmentation	Region 1	Region 2	Region 3	Region 4	Region 5
Leading edge	2, 3, 2, 1	2, 3, 2, 1	2, 2, 1	2, 2, 1	2, 2, 1
Leading edge panel	2, 3, 2, 1	2, 6, 3, 2, 1	2, 6, 2, 1	2, 6, 2, 1	–
Main beam	2, 3, 2, 1	2, 4, 3, 2, 1	2, 4, 2, 1	2, 4, 2, 1	2, 4, 2, 1
Trailing edge panel	2, 3, 2, 1	2, 7, 3, 2, 1	2, 7, 2, 1	2, 7, 2, 1	–
Trailing edge strengthening	2, 3, 2, 1	2, 7, 5, 3, 2, 1	2, 7, 5, 2, 1	2, 7, 2, 1	–
Trailing edge	2, 3, 2, 1	2, 7, 5, 3, 2, 1	2, 2, 1	2, 2, 1	2, 2,1
Web	–	9, 8, 9	9, 8, 9	9, 8, 9	–

Region 1: 0–1.366 m, Region 2: 1.366–10.25 m, Region 3: 10.25–43.05 m, Region 4: 43.05–61.5 m, Region 5: improved blade tip design;
1: gelcoat, 2: triaxial skin, 3: blade root triaxial skin, 4: carbon fiber, 5: fiber reinforced plastics, 6: leading edge foam, 7: trailing edge foam, 8: web foam, 9: biaxial skin.

$$T_b = L_b\cos\alpha + D_b\sin\alpha \tag{2}$$

$$P_b = \omega_{tip}\cdot M_b \tag{3}$$

where L_b is the blade lift force, D_b is the blade drag force, α is the angle of attack, and M_b is the blade torque.

To quantitatively characterize the aerodynamic performance of FOWT, the non-dimensionalized thrust coefficient (C_T) and power coefficient (C_P) are introduced, defined as [49,50]:

$$C_T = \frac{2T_b}{\rho_f A_s V_f^2} \tag{4}$$

$$C_P = \frac{2P_b}{\rho_f A_s V_f^3} = \frac{2M_b\cdot\omega_{tip}}{\rho_f A_s V_f^3} \tag{5}$$

where ρ_f is the incoming flow density and A_s is the swept area of the rotor.

3. Numerical method

3.1. FSI strategy

This study employs a coupled CFD (implemented in STAR-CCM +) and FEM (implemented in ABAQUS) co-simulation approach to establish

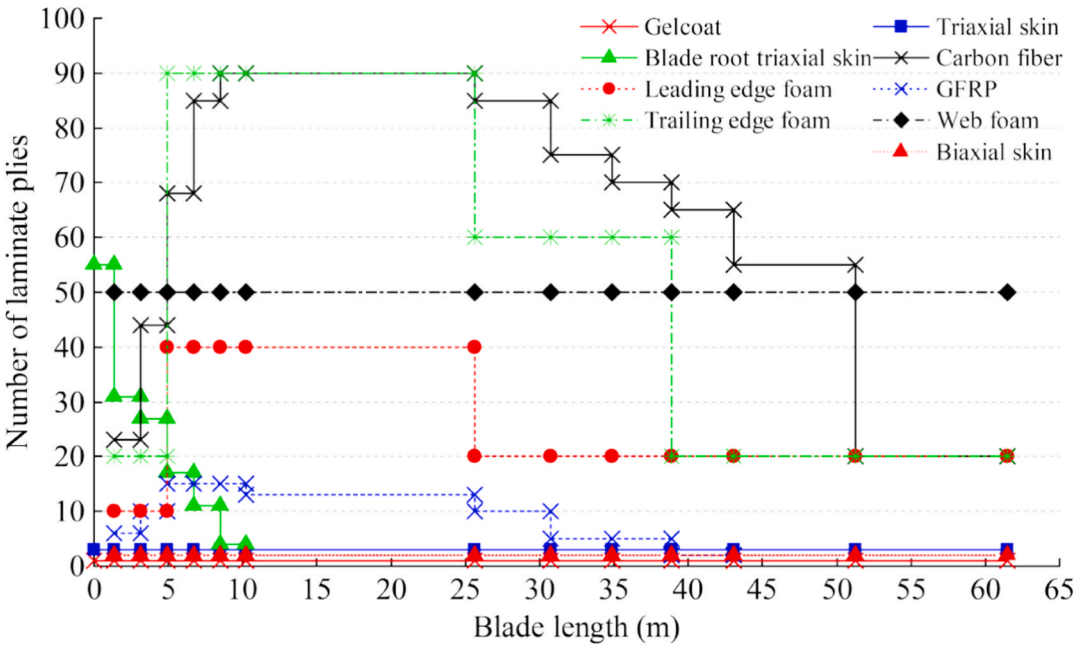

Fig. 4. Number of laminate plies along the blade spanwise.

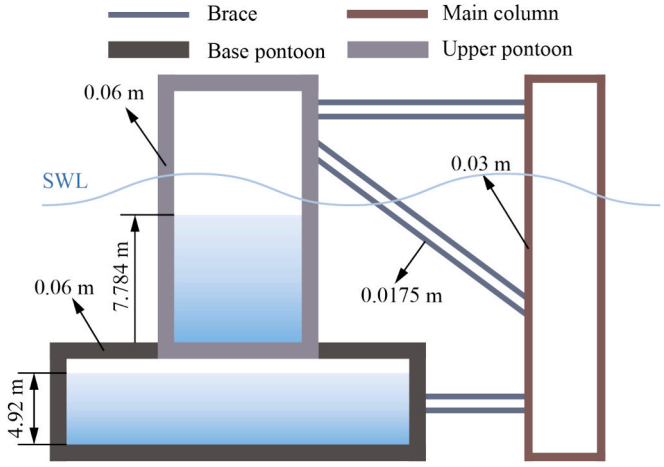

Fig. 5. The material and ballast distribution of the platform.

Table 4
Specific parameters of the OC4 semi-submersible platform CAE model.

Parameters	CAE model	Results in Ref. [40]	Deviations
Gross mass	1.3473×10^7 kg	1.3473×10^7 kg	–
Height of COM	6.54 m	6.54 m	–
Ballast height in upper pontoon	7.784 m	7.83 m	−0.59 %
Ballast height in base pontoon	4.92 m	5.0478 m	−2.53 %
Inertia moment about COM (I_{xc})	6.50×10^9 kg·m^2	6.827×10^9 kg·m^2	−4.79 %
Inertia moment about COM (I_{yc})	6.50×10^9 kg·m^2	6.827×10^9 kg·m^2	−4.79 %
Inertia moment about COM (I_{zc})	1.16×10^{10} kg·m^2	1.226×10^{10} kg·m^2	−5.38 %

Table 5
Specific properties of the mooring.

Parameters	values
Relaxation length	835.5 m
Diameter	0.0766 m
Equivalent mass density	113.35 kg·m^{-1}
Young's modulus	1.366×10^{14} Pa
Poisson's ratio	0.3
Tangential friction coefficient	0.74
Added mass coefficient	1
Transverse inertia coefficient	1
Transverse drag coefficient	1.1

a two-way FSI model for FOWTs, with the numerical modeling strategy shown in Fig. 6.

- Within the CFD framework, the Reynolds-averaged Navier-Stokes (RANS) equations are solved using a second-order implicit time discretization scheme to capture unsteady flow dynamics. A segregated flow solver employing a pressure–velocity coupling algorithm is used to ensure mass conservation throughout the solution process. The SST k-ω turbulence model is used to resolve near-wall boundary layer behavior and dynamic stall on turbine blades, while the volume of fluid (VOF) method captures air–water interfaces to simulate wind-wave coupling effect. The overset mesh and morphing mesh techniques are adopted to achieve the nonlinear dynamic responses of the FOWT.
- In the FEM framework, the multi-body dynamics method is used to describe the coupled motions of the subcomponents, with the implicit dynamics method employed to solve both global dynamic responses and local mechanical behaviors. The AQUA module in ABAQUS, integrated with Morison's equation, is used to account for hydrodynamic loads on the mooring system, including buoyancy, drag, and inertial forces [51].
- The coupling between the CFD and FEM solvers is achieved using the SIMULIA Co-Simulation Engine to enable real-time data exchange during transient simulations [52]. In this framework, the CFD solver

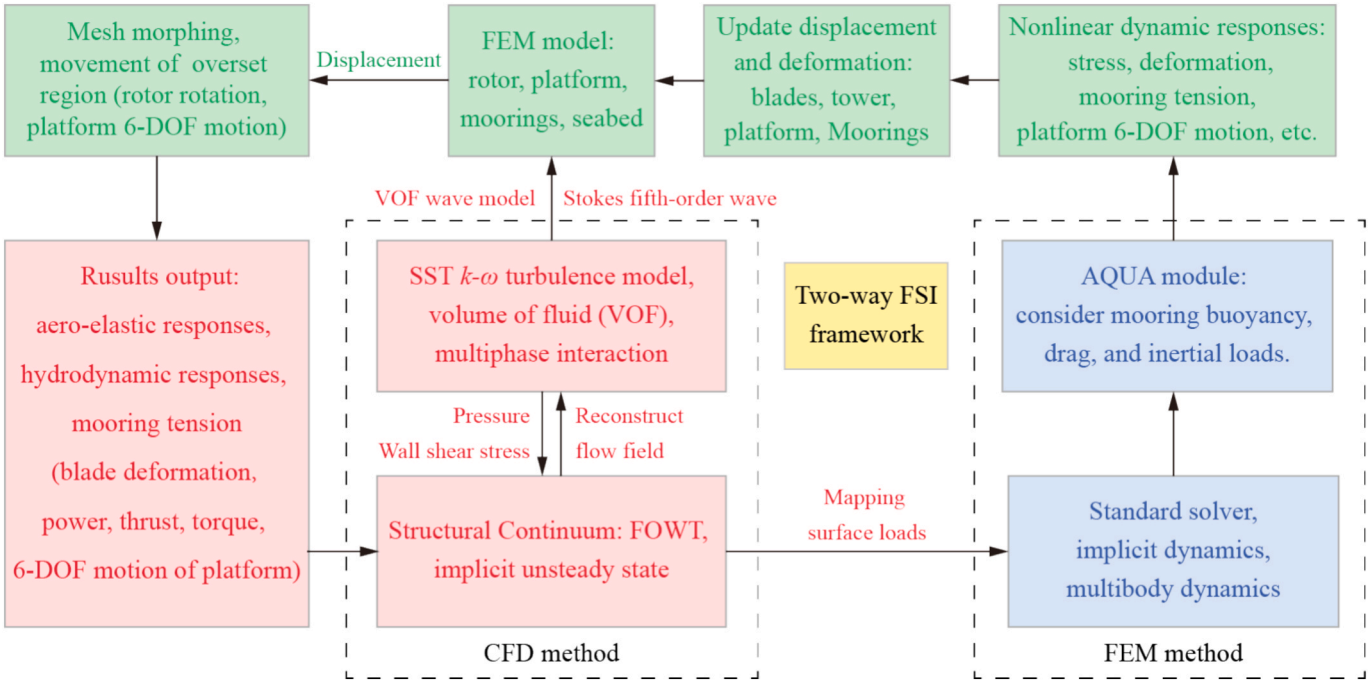

Fig. 6. The two-way FSI framework of the FOWT.

provides the pressure and wall shear stress acting on the structural surfaces, which are transferred to the FEM solver by the co-simulation interface. Simultaneously, the FEM solver conducts nonlinear dynamic analysis and feeds the resulting structural displacements back to the CFD solver to update the fluid mesh accordingly. The explicit coupling scheme manages data exchange frequency at each timestep to address large-scale transient and strongly nonlinear coupling scenarios of the FOWT. During each data transfer, spatial interpolation and consistent mapping are performed to maintain the accuracy and integrity of the exchanged information.

The proposed two-way FSI strategy enables comprehensive analysis of nonlinear coupled aero-elastic-hydro-mooring dynamic behaviors in FOWTs, providing critical insights for system optimization and extreme load assessment.

3.2. VOF waves model

The VOF wave model predicts the distribution and motion of immiscible phase interfaces by defining a volume fraction (a proportion of a specific phase within each grid cell) and performing convective transport of the volume fraction using the velocity field [53]. This model can accurately resolve the position and morphology of phase interfaces under sufficient grid resolution. In this study, the multiphase flow involves air and water, where the phase distribution and interface location are described by the water volume fraction field α_w:

$$\alpha_w = \frac{V_w}{V} \tag{6}$$

where V_w is the volume of water within the grid cell, and V is the total volume of the grid cell. When $\alpha_w = 0$, the cell contains air exclusively; when $\alpha_w = 1$, the cell is fully occupied by water; when $0 < \alpha_w < 1$, the cell contains an air–water interface.

The grid cells containing interfaces are treated as mixtures, with homogenized density ρ_h and dynamic viscosity μ_h defined as:

$$\rho_h = (1-\alpha_w)\rho_a + \alpha_w\rho_w \tag{7}$$

$$\mu_h = (1-\alpha_w)\mu_a + \alpha_w\mu_w \tag{8}$$

where subscripts a and w denote air and water, respectively.

The VOF transport equation is formulated as:

$$\frac{\partial}{\partial t}\int_V \alpha_w dV + \oint_A \alpha_w \mathbf{V_h}\cdot d\mathbf{S} = \int_V \left(Q_{\alpha_w} - \frac{\alpha_w}{\rho_w}\frac{d\rho_w}{dt}\right)dV - \int_V \frac{1}{\rho_w}\nabla\cdot(\alpha_w\rho_w\mathbf{V_d})dV \tag{9}$$

where $\mathbf{V_h}$ is the mixture velocity vector, $\mathbf{S}$ represents the surface area vector, $\mathbf{Q}$ is a user-defined source term for water phase, and V_d denotes the diffusion velocity.

3.3. Mooring model

The AQUA module in ABAQUS is a hydrodynamic analysis tool specifically designed for marine engineering structures. Its core functionality is based on the Morison equation, which introduces hydrodynamic loads to simulate the interaction between slender structures and the marine environment. In this study, the mooring system is modeled using hybrid beam elements, with distributed loads along the axial direction and inertial loads at cross-sectional variations applied by the AQUA module [54]. The distributed loads are decomposed into a transverse component perpendicular to the beam axis and a tangential component along the axial direction. The transverse and tangential drag forces per unit length of the hybrid beam element can be defined as:

$$F_{\mathrm{tr}} = 0.5\rho_{\mathrm{d}}C_{\mathrm{tr}}D_{\mathrm{b}}\Delta\mathbf{V_{tr}}(\Delta\mathbf{V_{tr}}\cdot\Delta\mathbf{V_{tr}})^{0.5} \tag{10}$$

$$F_{\mathrm{ta}} = 0.5\rho_{\mathrm{d}}C_{\mathrm{ta}}D_{\mathrm{b}}\pi\Delta\mathbf{V_{ta}}|\Delta\mathbf{V_{ta}}|^{\mathrm{m}-1} \tag{11}$$

where ρ_{d} is the fluid density, C_{tr} and C_{ta} represent the transverse and tangential drag coefficients, D_{b} denotes the characteristic length, $\Delta\mathbf{V_{tr}}$ and $\Delta\mathbf{V_{ta}}$ are the relative transverse and tangential fluid velocities, and m is the tangential drag exponent.

The inertial force per unit length on the beam element is defined as:

$$F_{\mathrm{ti}} = 0.25\rho_{\mathrm{d}}D_{\mathrm{b}}^2\pi\left[C_{\mathrm{ti}}(\mathbf{a_w} - \mathbf{a_w}\cdot\mathbf{ii}) + C_{\mathrm{tam}}\left(\mathbf{a_f} - \mathbf{a_f}\cdot\mathbf{ii}\right)\right] \tag{12}$$

where C_{ti} and C_{tam} are the transverse inertial and added mass coefficients, $\mathbf{a_w}$ and $\mathbf{a_f}$ represent the fluid accelerations with and without wave effects respectively, and $\mathbf{i}$ is the axial unit vector at a point on the beam element.

3.4. Boundary condition and mesh division

The FSI simulation boundary conditions for the FOWT are shown in Fig. 7. Fig. 7(a) presents the CFD-side boundary conditions, where the computational domain dimensions are non-dimensionalized using the rotor diameter ($D_r = 126$ m). A two-phase air–water flow is generated at the upstream velocity inlet through the VOF wave model, with air density set to 1.225 kg/m^3 and wind speed to 11.4 m/s, while water density is defined as 1025 kg/m^3. The fifth-order Stokes wave propagates from the air–water interface at the velocity inlet toward the pressure outlet. During propagation, the damping wave absorption model is applied to suppress vertical oscillations at the pressure outlet, thereby preventing far-field wave reflections from interfering with the FOWT dynamic response [55]. Additionally, overset domains (the rotating and moving domains) are employed to simulate wind turbine rotation and platform 6-DOF motions. To minimize mesh redundancy and enhance computational accuracy, the overset domains are designed to match the geometry of the FOWT. Three overset interfaces are ultimately established: between the rotating domain and computational domain (overset interface 1), the moving domain and computational domain (overset interface 2), and the rotating domain and moving domain (overset interface 3).

Fig. 7(b) depicts the FEM-side boundary conditions, focusing on the FOWT, mooring system, and seabed. In the FEM model, the mooring lines (MLs) are modeled as beam elements subjected to hydrodynamic loads from the AQUA module, with frictional contact effects between the mooring and seabed explicitly considered. Furthermore, the MLs are connected to fairleads and anchor points through joint connections to enable 3-DOF rotational motions. The wind turbine rotor achieves single-DOF rotation about the shaft axis through a hinge connection between the coupling points inside the hub and the nacelle. The rotational speed gradually increases from 0 to the rated speed (12.1 rpm) during simulation. In addition, the global gravity load is applied throughout the FEM model.

Fig. 8 presents the meshing results of the FOWT numerical model. In Fig. 8(a) (CFD model), the trimmed mesh technique is employed to handle complex surfaces for high-quality grid generation. The mesh size of the background domain is set to 10 m, whereas a finer mesh size of 1.25 m is applied in both the rotor rotation and the platform motion domains. A gradual mesh refinement strategy is adopted to ensure a smooth transition between regions of the computational domain. To accurately capture the flow characteristics near the blade's boundary layer, 16 prism layers are constructed on blade surfaces with a total thickness of 0.2 m and a first-layer grid height of 5×10^{-4} m. The maximum $y+$ value near the blade tip reaches approximately 106,

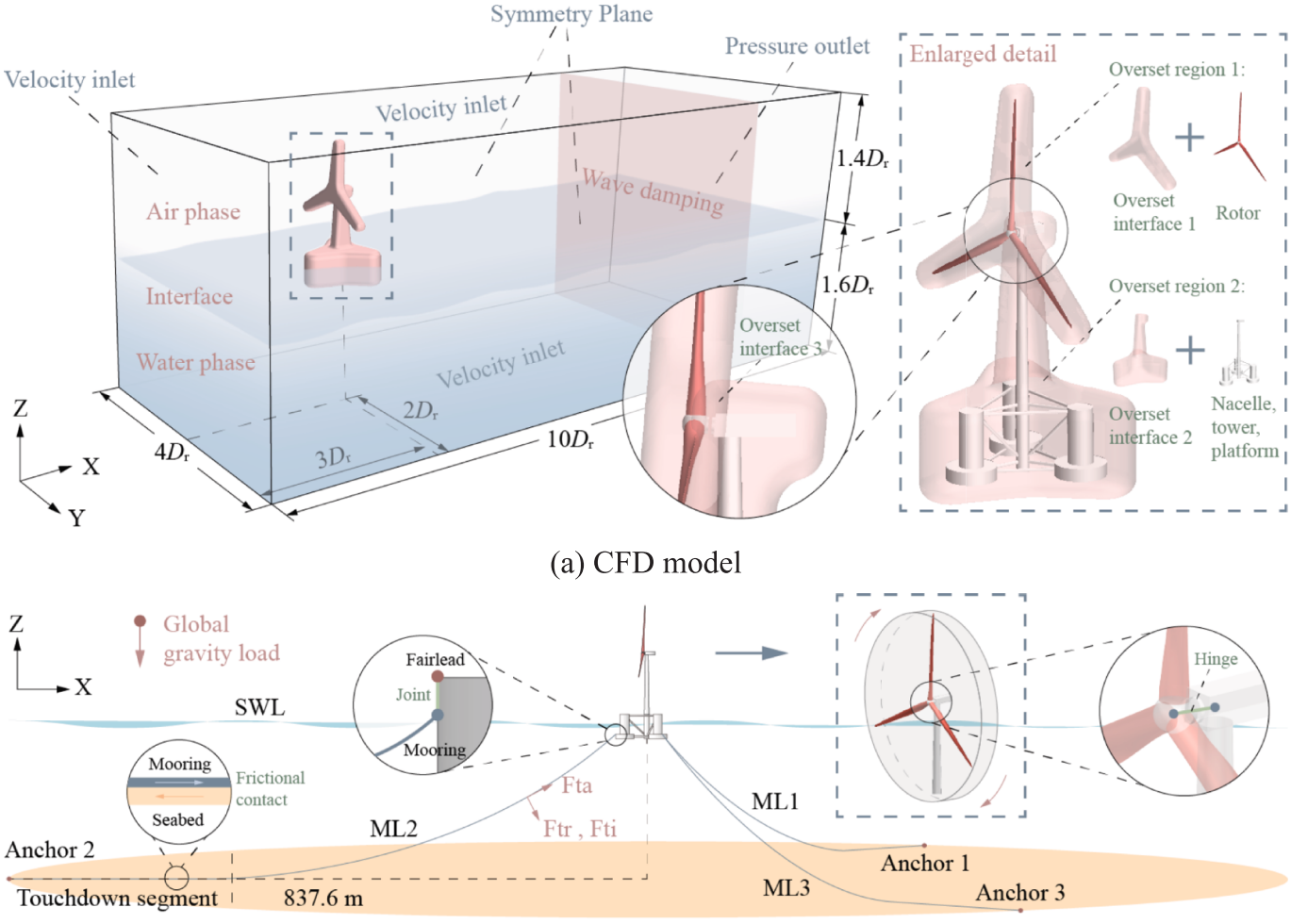

Fig. 7. The boundary conditions of CFD model and FEM model.

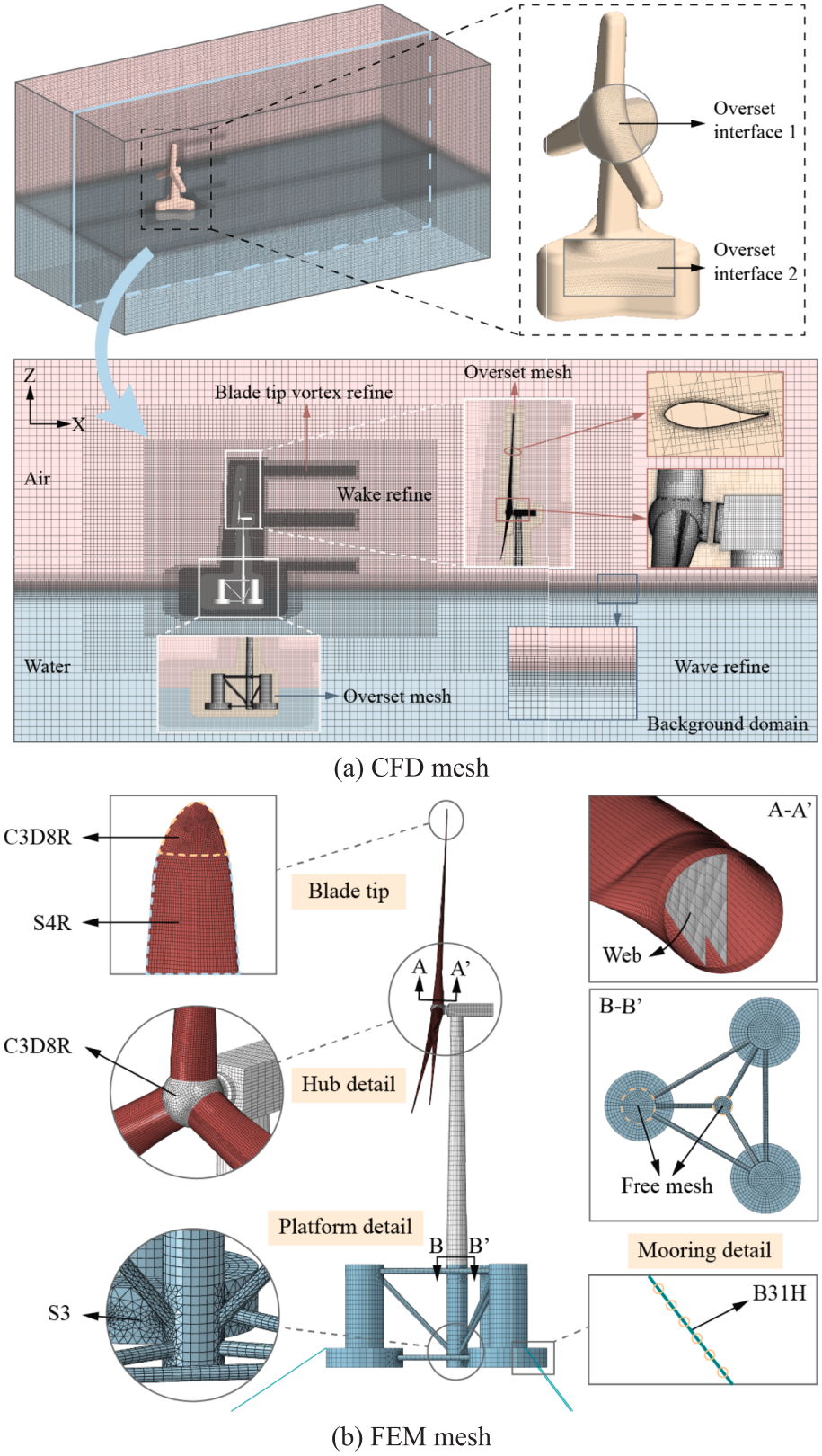

Fig. 8. Mesh distributions of CFD model and FEM model.

which is acceptable under the All $y+$ Wall Treatment employed in STAR-CCM + . This approach enables automatic switching between low and high $y+$ formulations based on local mesh resolution, balancing near-wall modeling accuracy and computational efficiency for full-scale modelling. Furthermore, additional mesh refinement is performed in regions near the tip vortices, root vortices, and hub connections to precisely resolve the evolution of the wake. The anisotropic mesh refinement at the air–water interface is essential for accurate wave generation. Within the wave propagation region, 20 layers of mesh are distributed along the Z-direction, while the mesh size in the X and Y

directions is uniform and ensured a resolution of at least 80 grids per wavelength. The rotational motion of the rotor and the 6-DOF motion of the platform are implemented by overset mesh technology combined with deforming mesh technology. The final CFD model generates a total of 19,806,395 grid nodes, with 6,313,174 in the rotor overset domain, 1,777,623 in the platform overset domain, and 11,715,598 in the background domain. Fig. 8(b) shows the meshing results of the FEM model, in which high-quality quadrilateral structured elements (S4R) are predominantly generated through surface partitioning and refinement of the FOWT geometry. In region with complex geometric such as blade tips, hubs, and cross-brace connections, unstructured meshing is applied using either linear hexahedral elements (C3D8R) or triangular shell elements (S3) depending on the local topology. The mooring system is modeled using hybrid beam elements (B31H). Table 6 summarizes the element types and the number of elements for each subcomponent of the FEM model.

During the two-way FSI calculation, both STAR-CCM + and ABAQUS were synchronized with a uniform time step of 0.01377 s, corresponding to one-degree angular rotation of the rotor per step. The simulation was conducted on the Barkla High Performance Computing (HPC) facility at the University of Liverpool, using two compute nodes with a total of 332 CPU cores (168 cores per node). A total of 522,875 coupled iterations were performed, and the computation was completed in approximately 348 h.

4. Numerical model validation

4.1. Aero-structural dynamics validation

4.1.1. Mesh independence

In CFD simulations, accurately solving the aerodynamic performance of the rotor and the vortex wake distribution is critical. For this purpose, the parametric regulation of the entire computational domain mesh is carried out using relative dimensions, and the mesh independence analysis is performed through the power coefficient (C_P) (Fig. 9). It is apparent that, as the number of grid nodes increases, the value of the C_P of the 5 MW wind turbine exhibits a slowing growth trend. When the number of grid nodes increases to 8.12×10^6, the absolute deviation between the C_P result obtained and the reference value corresponding to 10.29×10^6 nodes is 2.61 %, which meets the accuracy requirements. To conserve computational resources, the computational grid with 8.12×10^6 nodes is adopted in the following to solve the aerodynamic performance of the 5 MW wind turbine.

To ensure that the FEM model accurately resolves the structural dynamic response, a linear buckling analysis is performed by applying fixed loads to the pressure and suction surfaces of an individual 5 MW blade to validate the buckling deformation under varying mesh sizes (Fig. 10). Taking the buckling factor at a mesh size of 0.06 m as the reference, the deviation of the first-order buckling mode gradually decreases as the mesh size is refined. When the deviation in the buckling factor caused by mesh size changes remains below 5 %, the model is considered sufficiently accurate [45]. By considering both computational efficiency and accuracy, the mesh size of 0.12 m is ultimately selected, resulting in a 4.96 % deviation in blade buckling mode with a total of 44,994 elements.

Table 6
Element type distribution for each subcomponent of the FEM model.

	Rotor	Tower and nacelle	Platform	Mooring	Seabed
Element type	C3D8R + S4R	S4R	S4R + S3	B31H	C3D8R
Element number	4,968, 132,321	6,168	12,974, 5,334	2,508	1,176
Proportion	0.030, 0.80	0.037	0.078, 0.032	0.015	0.007

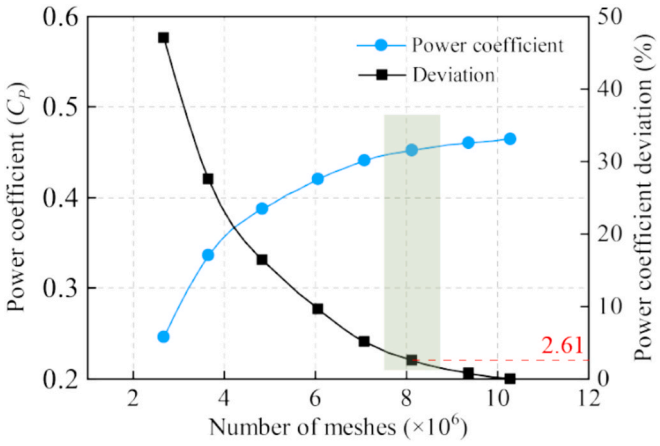

Fig. 9. Power coefficient deviation of 5 MW wind turbine.

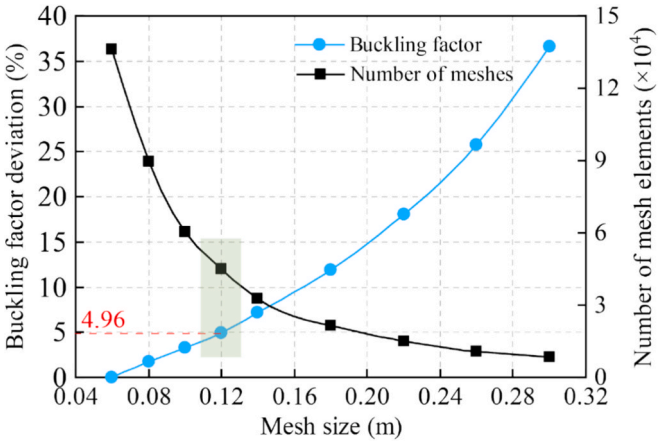

Fig. 10. Buckling factor deviation of 5 MW blade.

4.1.2. Aerodynamic performance

The power output of the 5 MW wind turbine is calculated over the full operating wind speed range (3 ~ 25 m/s). The results are compared with data from NREL [43] and Cheng et al. [55] to evaluate the reliability of the CFD model, as shown in Fig. 11. In the below-rated region (wind speed up to the 11.4 m/s), the present CFD results show good agreement with the reference data. At wind speed above the rated value, blade pitch control is required to ensure the safe and stable operation of the wind turbine. The CFD predicted power output is slightly higher than those from NREL benchmark. However, the deviation remains within an acceptable range. These results confirm that the CFD model used in this study provides a reliable and accurate basis for aerodynamic

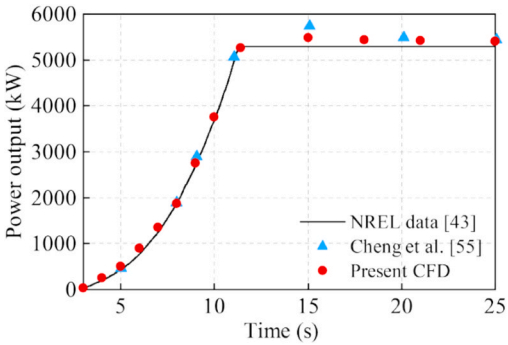

Fig. 11. Comparison of average power output over the full wind speed range.

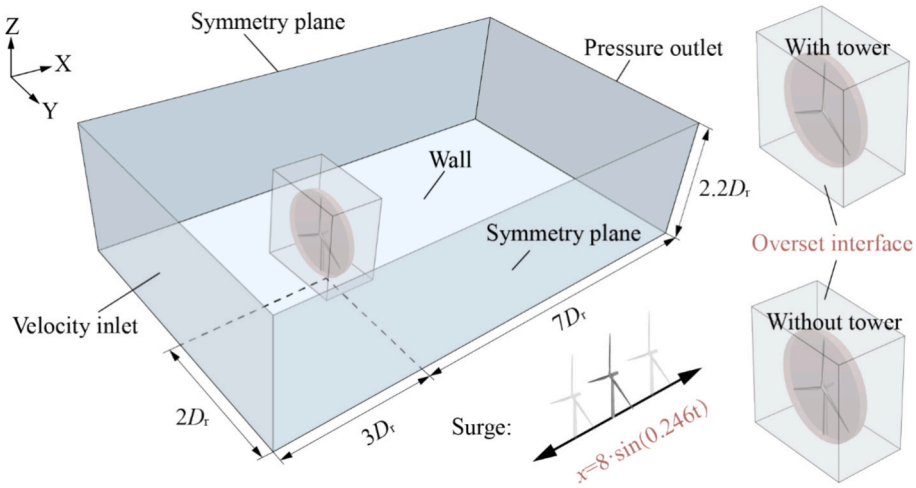

Fig. 12. Boundary conditions for the 5 MW wind turbine under surge motion.

performance prediction.

To further validate the numerical accuracy under dynamic inflow conditions, a prescribed sinusoidal platform motion is applied in an uncoupled simulation. The boundary conditions are illustrated in Fig. 12. The inflow wind speed was set to the rated value, and a surge motion with an amplitude of 8 m and an angular frequency of 0.246 rad/s is imposed using the overset mesh technique. In addition, simulations are performed with and without tower interference to assess its impact on the power coefficient of the rotor.

The power coefficient (C_P) of the 5 MW wind turbine under prescribed surge motion is compared with the results obtained by Tran et al. [56] to validate the reliability of aerodynamic performance prediction under uncoupled conditions, as shown in Fig. 13. The results indicate that the surge motion induces periodic fluctuations in the C_P response. When the tower is not considered, the C_P curve exhibits a smooth fluctuation trend. However, when the tower is included, pronounced drops in C_P occur each time a blade passes in front of the tower due to the tower shadow effect. Additionally, the values obtained by the traditional BEM and GDW methods are generally lower than those from the CFD approach. From a numerical perspective, the unsteady CFD method comprehensively accounts for viscous flow separation and vortex wake interactions around the rotor, tower, and nacelle, thereby achieving higher accuracy.

4.1.3. Modal analysis

The modal analysis reveals key parameters such as natural frequencies, mode shapes, and damping ratios under free vibration conditions for the blade, effectively preventing resonance within specific frequency bands. The modal analysis is performed on the 5 MW blade with fully fixed constraints at the root to obtain its natural frequencies and mode shapes, which are then compared with the results obtained by Deng et al. [57], as summarized in Table 7. Due to differences in the reference surfaces for layup and blade tip modeling, minor

Table 7
Comparison of the first 6 natural frequencies.

Order	Frequency (Hz) Deng et al. [57]	Present result	Deviation	Type	Mode shape
1	0.86	0.83	−3.49 %	1st flapwise	
2	1.10	1.13	+2.73 %	1st edgewise	
3	2.72	2.60	−4.41 %	2nd flapwise	
4	3.94	4.03	+2.28 %	2nd edgewise	
5	5.51	5.33	−3.27 %	3rd flapwise	
6	6.36	6.24	−1.89 %	1st torsion	

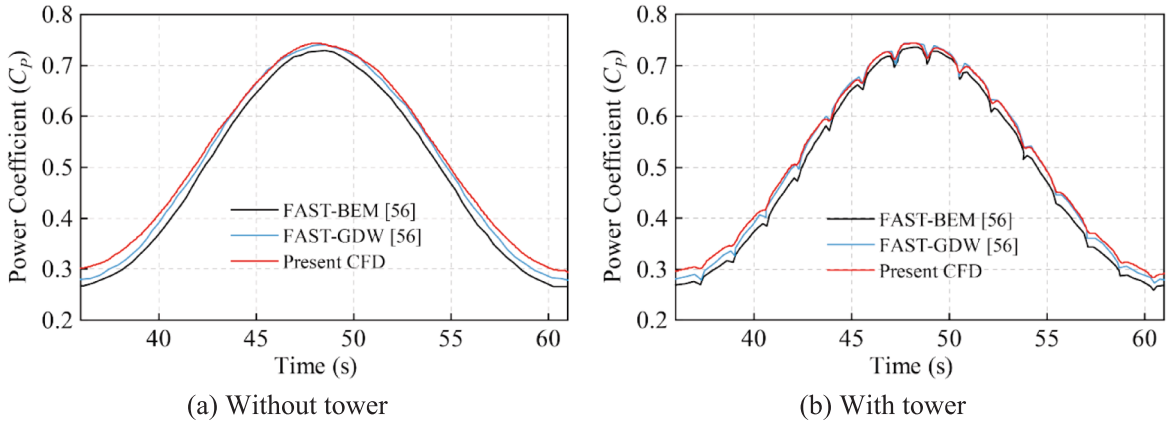

Fig. 13. Aerodynamic performance verification of the 5 MW wind turbine under surge motion.

deviations (<5%) exist between the first six natural frequencies of the present FEM model and the reference data. These discrepancies remain within acceptable ranges, demonstrating the high reliability of the FEM model adopted.

4.2. Two-way FSI framework validation

Free decay tests of the FOWT are conducted using a two-way FSI framework, as depicted in Fig. 14. On the fluid side, the VOF wave model is employed to simulate still water, with zero wind velocity applied above the free surface. On the structural side, the full FOWT assembly is modeled, including the rotor, nacelle, tower, and platform. The corresponding mass properties are summarized in Table 3 of Section 2.2.1. The mooring system is modeled using hybrid beam elements, and frictional contact interaction between the mooring lines and the seabed is taken into account. Consequently, the free decay motion of the FOWT is realized by imposing predefined initial conditions on the structure side, specifically a surge displacement of 22 m and a pitch angle of 8 deg.

The free decay tests of the FOWT are performed under both frictional and frictionless contact conditions using the FSI framework. The results are compared with those obtained by Tran et al. [56] using the FAST and DFBI methods, as shown in Fig. 15. The pitch and surge decay responses from different numerical approaches exhibit good agreement in overall trend, with some discrepancies in amplitude and decay period. For the surge decay response, the FSI results closely match those from FAST when frictional contact is not considered. When frictional contact is included, the added damping leads to a noticeable reduction in the surge amplitude. Furthermore, the presence of frictional contact delays mooring restoring force and changes the effective stiffness, resulting in a longer surge decay period. In contrast, the DFBI method, which uses a quasi-static catenary model, fails to account for seabed friction, transverse inertial moments, and buoyancy of the mooring lines, leading to deviations from realistic behavior. Overall, the decay curves predicted by the different numerical methods are in good agreement, indicating that the two-way FSI approach and hydrodynamic validation adopted in this study are both reliable and reasonable.

5. Fully coupled results of FOWT

5.1. Aerodynamic performance

5.1.1. Response comparison

Under rated wind speed and regular wave conditions, a fully coupled FSI analysis is conducted for the FOWT. The power output and thrust results are compared with those of a 5 MW bottom-fixed wind turbine (BFWT), as shown in Fig. 16 (different background colors in the figure indicate various wave periods). It should be noted that the BFWT simulation is performed using CFD method without considering wind shear, and the air density is kept consistent with that used for the FOWT.

As shown in Fig. 16, both FOWT and BFWT exhibit three distinct drops in their C_P and C_T within a single rotor revolution, attributed to the effects of blade rotation and tower wake interference. The C_P and C_T responses of the FOWT display periodic fluctuations that correlate with the wave period, whereas those of the BFWT tend toward a steady state.

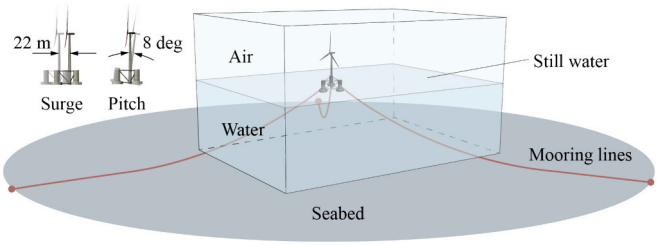

Fig. 14. Free decay tests of the FOWT within the two-way FSI framework.

This behavior arises from the periodic surge motion induced by wind-wave coupling in the FOWT, which alters the dynamic inflow conditions of the blades. The aerodynamic performance of FOWT exhibits an initial increasing and subsequent decreasing trend during the reciprocating motion of the platform from the upwind to the downwind orientation.

Moreover, the pitch motion coupled with surge motion generates periodic fluctuations in the blade angle of attack. This results in a highly non-uniform distribution of aerodynamic loads, ultimately exacerbating the amplitude of aerodynamic performance fluctuations. The enlarged detail reveals small-amplitude and high-frequency fluctuations in the C_P and C_T responses of the FOWT. These are attributed to the inclusion of structural dynamics in the present study, where geometric nonlinearities induced by low-order vibrations of the blades and tower further modify the local angle of attack, potentially leading to flow separation at the leading edge and even dynamic stall.

Unlike the BFWT, the dynamic interactions exist among the individual components of the FOWT. The closed-loop system comprising the platform, tower, rotor, and moorings introduces feedback mechanisms that amplify aerodynamic performance fluctuations. Table 8 compares average values, amplitudes, and standard deviations of C_P and C_T between the FOWT and BFWT. Over five wave periods, the average C_P and C_T of the FOWT are 0.436 and 0.716, respectively, showing decreases of 6.84 % and 3.50 % compared to the BFWT. The amplitude response results indicate that the aerodynamic performance of the FOWT is highly unstable, with standard deviations of C_P (0.022) and C_T (0.016) increasing by 340 % and 300 %, respectively, compared to the BFWT. This highlights the complexity of FOWT system dynamics and the associated design challenges, underscoring the necessity of establishing a reliable fully coupled aero-elastic-hydro-mooring numerical framework for FOWT analysis.

Fig. 17 presents the single-blade flapwise, edgewise, and torsional moment responses for the FOWT and BFWT (with different background colors distinguishing the blade rotation periods). The flapwise moment is the largest, followed by the edgewise and torsional moments – the reason being that aerodynamic lift acts perpendicularly to the blade chord line and aligns with the flapwise direction, which has a substantially larger moment arm (spanwise) compared to the edgewise (chordwise) direction, resulting in a flapwise moment significantly larger than the edgewise moment. The torsional moment is determined by pressure distributions on the blade's suction and pressure surfaces, with a moment arm comparable to the chordwise dimension in the edgewise direction. Due to the higher torsional stiffness, the torsional moment remains the smallest in magnitude.

By calculating the average blade moments over six rotation cycles, it is found that the average flapwise and torsional moments of the FOWT are 11.16 MN·m and 0.0933 MN·m, respectively, increasing by 12.16 % and 238.0 % compared to the BFWT. The primary reason for these results is that the FOWT considers the 6-DOF motions of platform and structural flexibility, continuously altering blade inflow conditions and local angles of attack. Such alterations induce large-scale flow separation, causing highly nonlinear load distributions across the blade suction and pressure surfaces, thus resulting in a more pronounced increase in torsional moment compared to the flapwise moment. The average edgewise moment of the FOWT is 1.19 MN·m, which represents an 11.19 % reduction compared to the BFWT. This discrepancy arises because the BFWT model employs rigid blades in the CFD simulations, resulting in negligible material and aerodynamic damping. In contrast, the elastic deformation of the FOWT blades and platform motion provide the conditions for generating damping mechanisms, allowing part of the edgewise load to be dissipated rather than fully transmitted to the hub. As is evident from the enlarged details, small-amplitude, high-frequency fluctuations are also present in the flapwise and edgewise moments of the FOWT blades; however, this characteristic is not prominent in the torsional moment response.

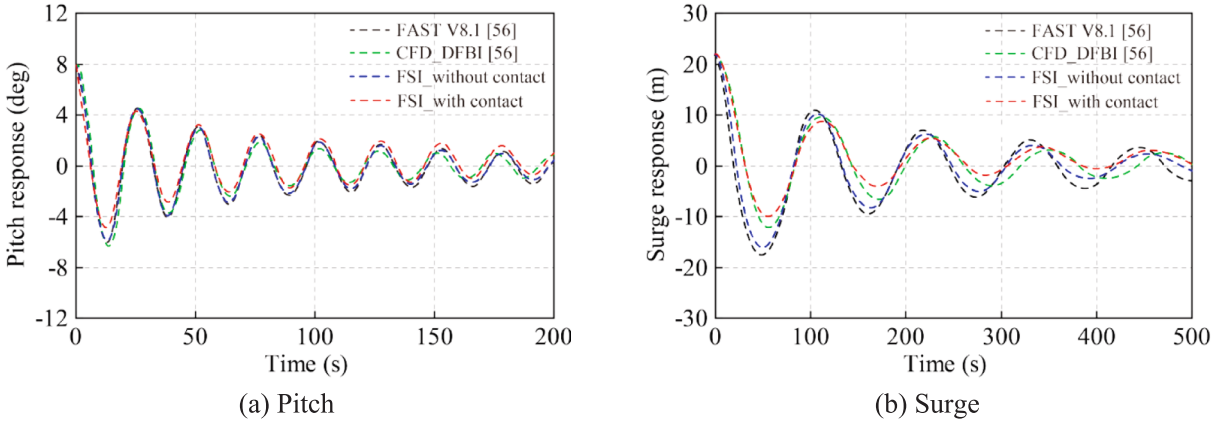

Fig. 15. Comparison of the free decay test results for the FOWT.

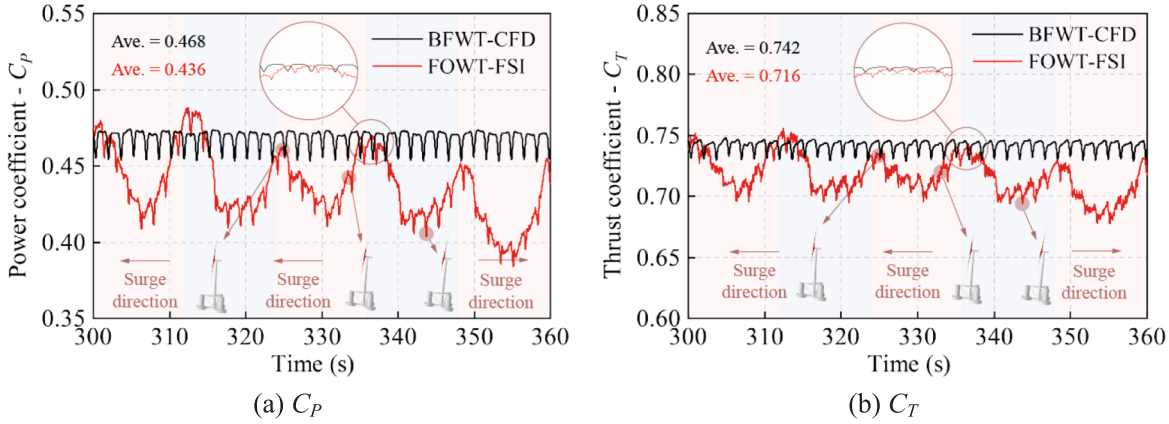

Fig. 16. Comparison of aerodynamic performance between FOWT and BFWT.

Table 8
Comparison of aerodynamic performance results of FOWT and BFWT.

Object	Average value		Amplitude		Standard deviation	
	C_P	C_T	C_P	C_T	C_P	C_T
BFWT	0.468	0.742	0.021	0.019	0.005	0.004
FOWT	0.436	0.716	0.104	0.078	0.022	0.016

5.1.2. *Flow field distribution*

Fig. 18 presents the flow field visualization results for the FOWT and BFWT at the Y = 0 m cross-section. As indicated in Fig. 18(a), the 6-DOF motions of the FOWT periodically alter the spatial orientation of the rotor plane, thereby affecting the stable formation of blade tip vortices. Before these tip vortices fully develop downstream, the inclination or translation of the rotor plane due to platform motions forces a shift in the vortex core positions, resulting in more densely packed vortex structures within the near-wake region. In contrast, the fixed tower of the BFWT allows the tip vortices to develop naturally in a stable flow environment, leading to increased spacing between vortex cores and their propagation downstream or even farther afield.

The enlarged details reveal that vortex shedding within the rotor-swept area occurs along most of the blade span. Under aeroelastic coupling, the non-uniform deformation and vibration along the spanwise of the FOWT blades cause periodic and large amplitude fluctuations in the local angle of attack. These high-frequency dynamic variations in the angle of attack are further amplified by the superimposed 6-DOF motions of the platform, resulting in multiple localized flow separations along the blade span and forming continuous vortex shedding bands.

The vorticity fields shown in Fig. 18(b) indicate that the FOWT exhibits more rapid vortex wake dissipation compared with the BFWT. Under wind-wave coupling, the platform 6-DOF motions and flexible blade deformations continuously alter inflow conditions across the rotor-swept area. Consequently, the vortex wake no longer develops in a stable, orderly manner; instead, it exhibits enhanced shear-layer disturbances and vortex interactions, significantly increasing turbulence intensity and wake dissipation rates. Simultaneously, platform motions and wave-induced free-surface fluctuations modify the vertical velocity gradients of the near field, accelerating vortex structures toward earlier turbulent mixing stages.

The velocity deficit in the wake region ($0.5 \sim 5D_r$) of the FOWT and BFWT is further analyzed through the velocity contour at Z = 90 m, as illustrated in Fig. 19. The 6-DOF motions of the FOWT directly alter the inflow conditions to the rotor plane and the initial momentum distribution in the wake. This leads to an asymmetric velocity gradient distribution in the wake shear layer accompanied by vigorous vortex shedding, thereby intensifying turbulent mixing between the wake and the surrounding high-speed free stream. Consequently, the velocity distribution at the outer boundary of the FOWT shear layer is higher than that of the BFWT. Moreover, it is evident that the wave-induced fluctuations of the free surface modify the vertical velocity gradient at the lower boundary of the wake, effectively enhancing turbulent mixing and disrupting the stable wake development downstream ($2 \sim 5D_r$). In comparison, the BFWT maintains a more coherent low-speed core and stable shear-layer structure in the wake due to its structural and inflow stability, lacking sufficient perturbations to facilitate turbulence transition. Therefore, the wake dissipation rate for the BFWT is slower, and the wake recovery distance is longer than that of the FOWT.

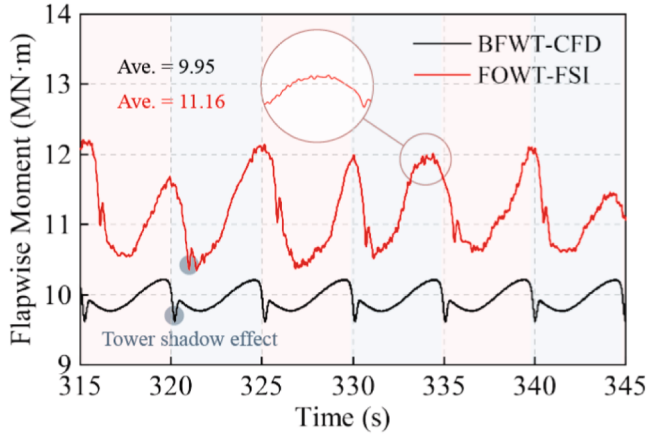

(a) Flapwise moment

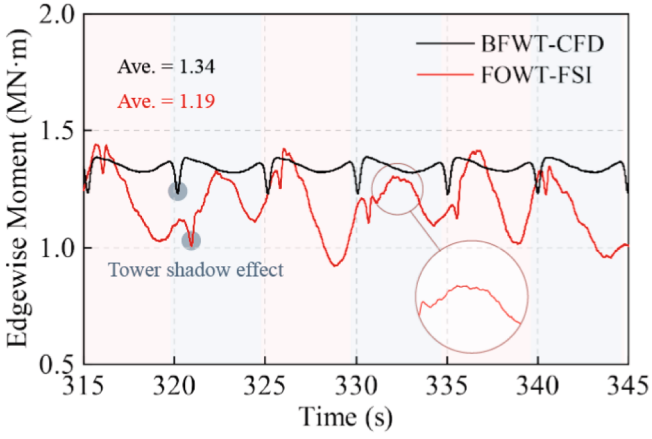

(b) Edgewise moment

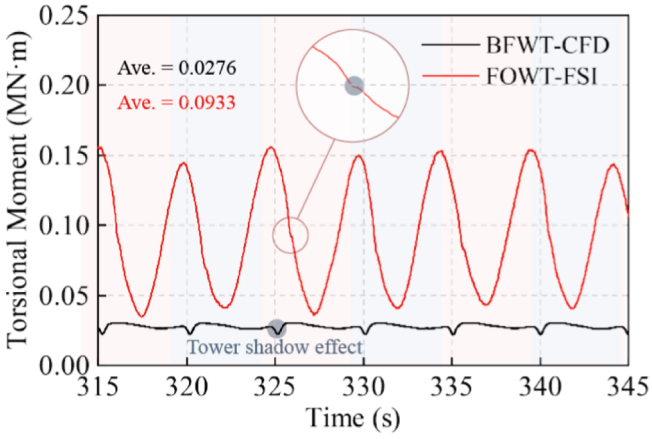

(c) Torsional moment

Fig. 17. Aerodynamic performance comparison of single blade.

The velocity distributions at various distances from the rotor hub center ($0.5 \sim 5D_r$) are obtained by placing velocity probes at hub height, as shown in Fig. 20. It is demonstrated that significant velocity deficits exist in the core region of the wake, with magnitudes gradually decreasing as the radial distance increases. Approaching the outer boundary of the shear layer, the velocity profiles begin to rise, eventually reaching the free-stream velocity due to turbulent mixing. In the near-wake region ($X/D_r = 0.5$), the velocity distribution in the FOWT wake is essentially symmetric, whereas the BFWT wake exhibits a distinct offset of its center. As the wake propagates downstream ($1 \leq X/D_r \leq 5$), the FOWT wake velocity distribution gradually becomes more irregular, with the wake center shifting toward the −Y-axis direction and experiencing greater velocity deficits compared to the + Y-axis. In contrast, the BFWT wake evolves more gradually, maintaining a coherent low-speed structure for an extended distance downstream. Moreover, due to the synergistic effect of waves and platform motions enhancing momentum exchange within the wake region, the wake velocities for the FOWT are consistently higher than those for the BFWT within the range $0.5 \leq X/D_r \leq 5$.

5.2. Hydrodynamic performance

5.2.1. Dynamic responses of platform

Under wind-wave coupling, the FOWT exhibits nonlinear 6-DOF dynamic responses. The mooring system maintains dynamic equilibrium in both translational and rotational motions by providing restoring forces and moments, ensuring the safe and stable operation. In the fully coupled model, moorings are modeled using hybrid beam elements, with seabed contact and friction effects taken into account. Aerodynamic loads also play a non-negligible role, primarily acting on the rotor and tower through thrust and moments, and are ultimately transmitted to the platform. The 6-DOF response from the fully coupled simulations under rated wind speed (11.4 m/s) and regular wave (height 7.58 m, period 12.1 s) are shown in Fig. 21, where dark lines parallel indicating average response levels.

Since the waves are initially upstream and wind speed ramps from zero, the pitch response (Fig. 21(a)) grows gradually before reaching a stable fluctuation state. The fluctuation period is dominated by the first-order high-frequency wave excitation force. The overturning moment induced by the combined wind and wave loads results in a certain pitch angle of the FOWT. After 120 s of calculation, the pitch angles fluctuation range lies between [2.47, 5.59] deg. When the pitch angle reaches 4.07 deg, the mooring restoring moment fully counteracts the overturning moment. Due to the periodic nature of wave loading, the FOWT undergoes reciprocating motion around this dynamic equilibrium point.

Figs. 21(b)~(c) show the roll and yaw responses of the FOWT, respectively. Since the wave direction is aligned with the X-axis, the roll response is not directly influenced by the wave excitation moment. Consequently, its maximum fluctuation amplitude over the entire response duration remains within a narrow range of [-0.49, 0.44] deg. However, the roll response exhibits a fluctuation frequency consistent with the wave period and shows a gradually increasing trend. In contrast, the low-frequency characteristics of second-order wave difference frequency forces (drift forces) more readily excites the yaw motion. These low-frequency forces cause slow platform drift motion, leading the FOWT to gradually deviate from the upwind direction around the Z-axis. Moreover, it can be observed that the yaw response exhibits a trend consistent with the roll response. This arises because the platform attitude change induced by roll and the resulting redistribution of aerodynamic thrust on the rotor indirectly influence the yaw response. Although the FOWT will eventually return to its equilibrium position under the restoring moment of the mooring system, the relatively weak yaw restoring stiffness results in both an increased fluctuation amplitude and a longer time to reach a steady state.

As shown in Fig. 21(d), the average heave response of the FOWT is −0.29 m, indicating that the overall draft depth remains consistent with the initial design value. In addition to high-frequency periodic fluctuations induced by first-order wave excitation forces, the heave motion also contains superimposed low-frequency components. A similar phenomenon is observed in the surge response (Fig. 21(e)), except that the surge reaches dynamic equilibrium only after approximately 120 s. This delay occurs because the surge motion aligns with the direction of combined wind and wave loading and is more strongly influenced by both wave excitation and drift forces. When the surge displacement reaches 6.98 m, the wave-induced force is fully balanced by the mooring restoring force.

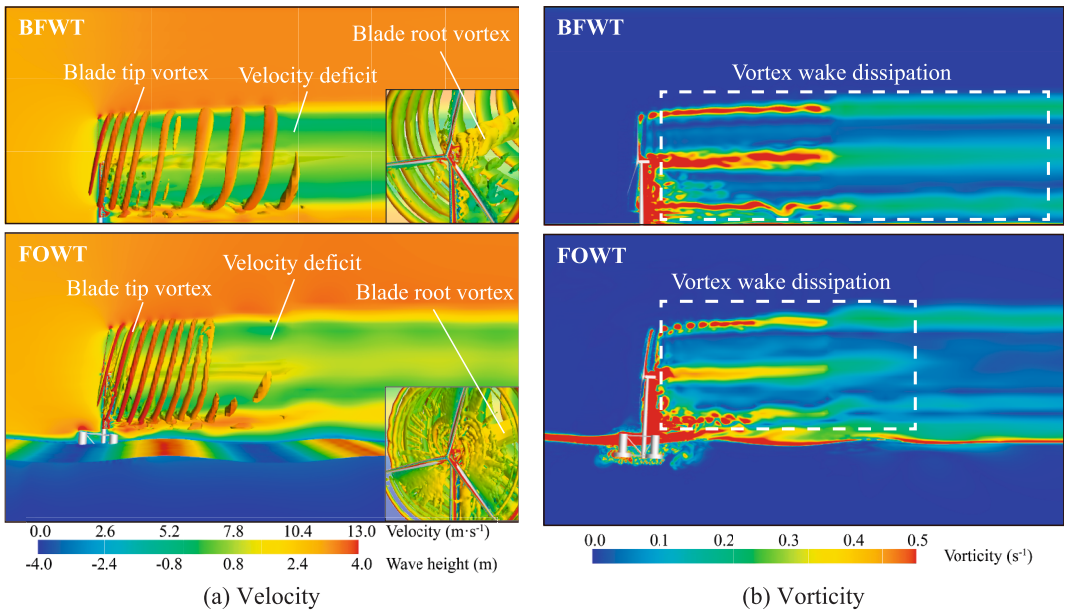

Fig. 18. Flow field distribution of the FOWT and BFWT.

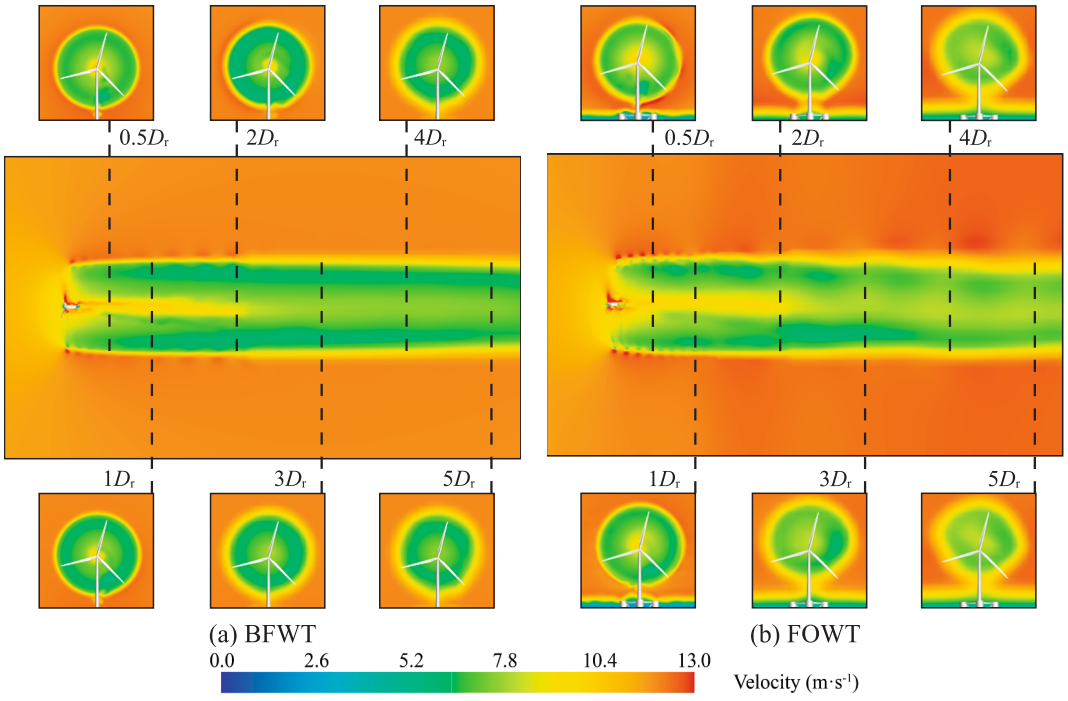

Fig. 19. Comparison of wake dissipation at Z = 90 m section.

Finally, similar to the roll response, the sway response is relatively insensitive to wave excitation forces, as shown in Fig. 21(f). Due to the interaction of nonlinear loads, the FOWT gradually drifts toward the −Y-direction during its surge motion, with a maximum sway amplitude range of [-2.47, 0.38] m.

5.2.2. *Mooring tension*

Fig. 22 shows the tension response trends of the FOWT mooring system. Since the direction of the connection line between the anchor (located along the −X-axis) and the fairlead aligns with the surge direction, ML2 experiences increased tension when the FOWT moves in the + X direction. By comparing with Fig. 21(e), it is evident that the trends of the surge motion and ML2 tension response are largely consistent. For ML1 and ML3, which are symmetrically positioned along the X-axis with anchor points located in the + X, their tension responses exhibit trends opposite to that of ML2. As shown in Fig. 21(f), the FOWT exhibits sway motion toward the −Y-direction, resulting in a more relaxed state for ML3 compared to ML1, and consequently a reduction in ML3 tension. When the sway motion approaches zero, the tension responses of ML1 and ML3 become nearly identical. Table 9 presents the maximum, average, and average amplitude values of mooring line tensions for ML1, ML2, and ML3. The average and amplitude results are based on data calculated after 120 s. As shown in Table 9, the mooring tension on the windward side (ML2) consistently remains at a higher

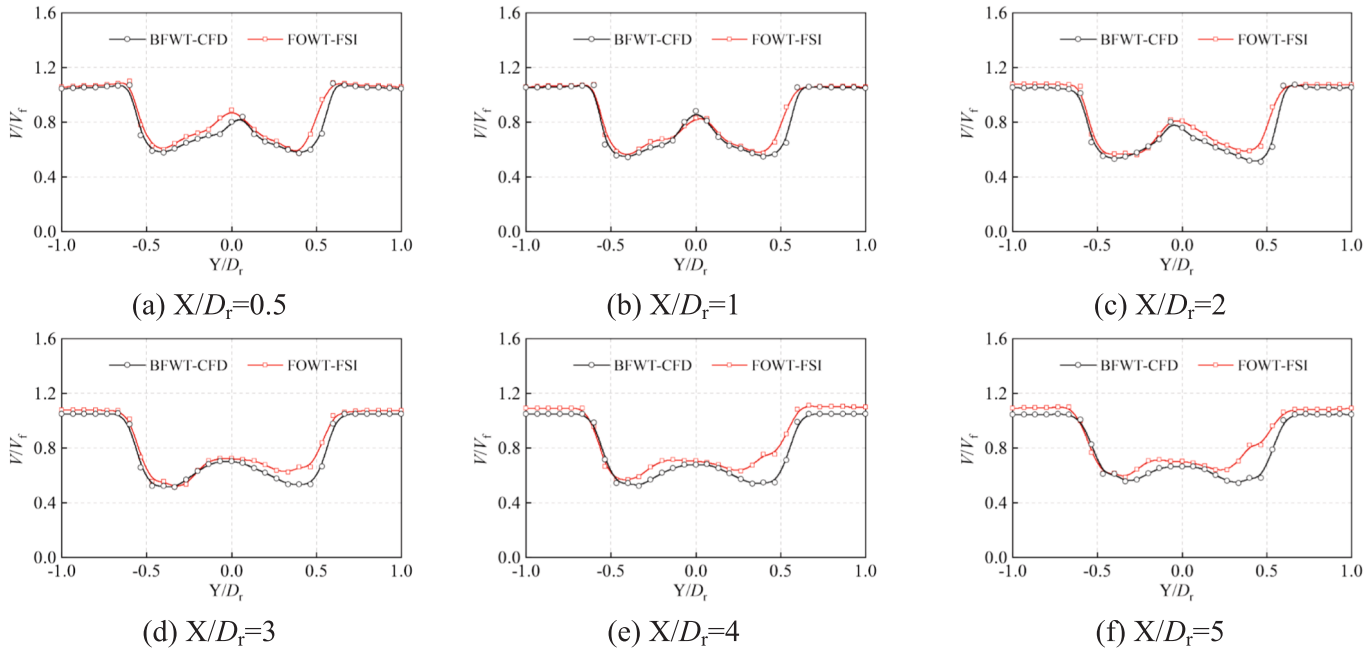

Fig. 20. Comparison of velocity deficit at hub height between FOWT and BFWT.

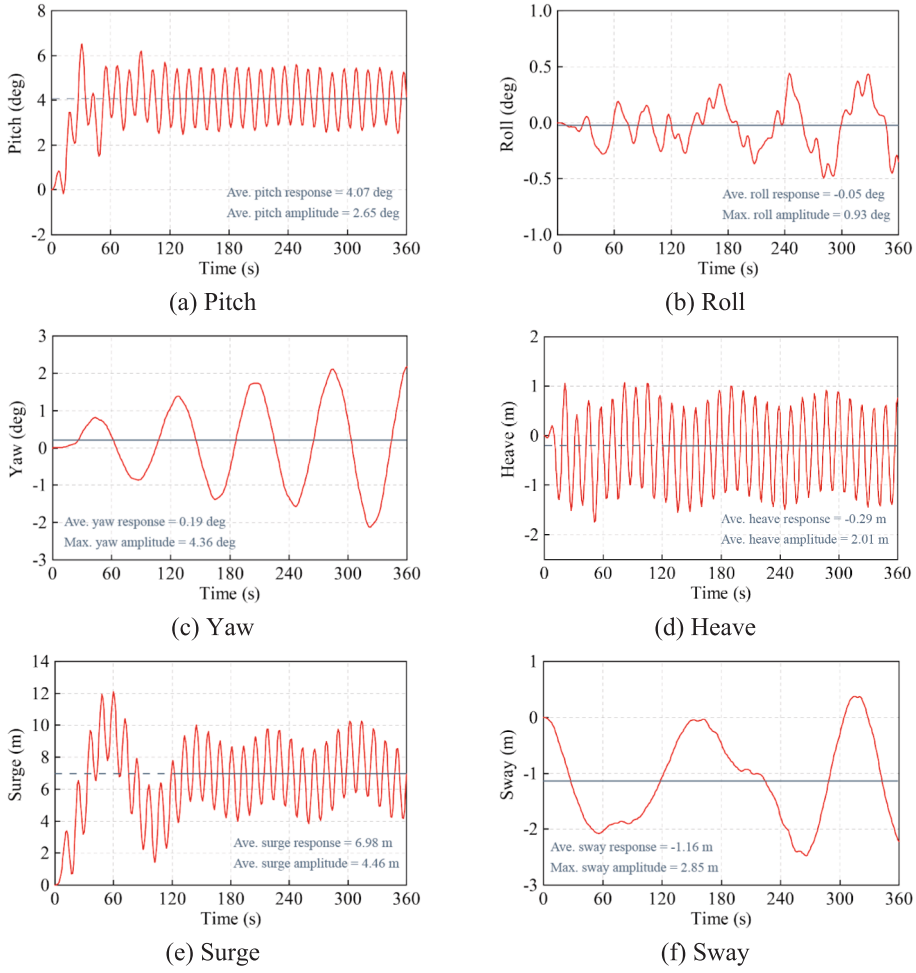

Fig. 21. 6-DOF response results of FOWT.

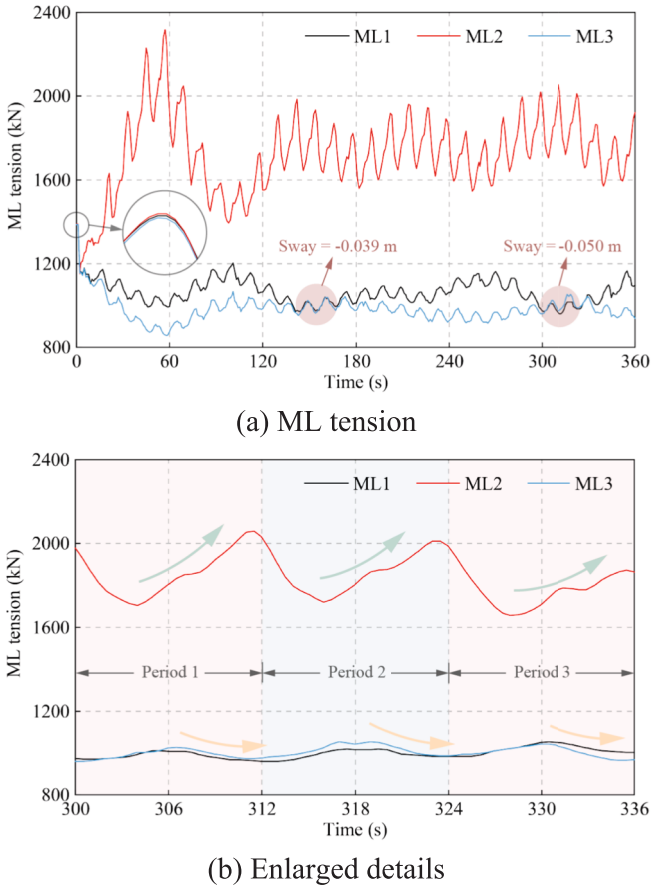

Fig. 22. ML tension responses of FOWT.

Table 9
Mooring tension response results of FOWT.

Object	Maximum value (kN)	Average value (kN)	Average amplitude (kN)
ML1	1388	1048	55.81
ML2	2317	1756	299.4
ML3	1385	979.0	56.24

level, with a maximum value of 2317 kN, corresponding to a maximum surge drift distance of 12.11 m. The average tension response amplitudes of ML1 and ML3 are 1048 kN and 979.0 kN, respectively, which represent reductions of 40.32 % and 44.25 % compared to ML2 (1756 kN).

5.3. Structural nonlinear response

5.3.1. Stress distribution and deformation

The structural dynamics of FOWTs are governed by complex coupling among wind-wave loads, structural characteristics, material stiffness, and dynamic responses. Fig. 23 shows the stress distribution and deformation response of the overall FOWT system. Under aerodynamic loading, the stress on the windward and leeward sides of the tower increases significantly, primarily due to the overturning moment generated by rotor thrust. As shown in Fig. 23(a), the stress on the windward side increases gradually from the tower top to its base. This occur because the tower behaves like a cantilever beam under wind loading, with bending moments increasing from zero at the top to a maximum at the base, where the stress reaches 1.02×10^8 Pa. Within the entire FOWT system, the maximum stress (2.87×10^8 Pa) occurs at the bottom of the platform's main column. This results from the combined concentrated mass load of the tower, nacelle, and rotor, as well as the effects of the platform's self-weight, hydrodynamic loads, and inertial forces induced by platform motion. Moreover, the horizontal and diagonal braces are responsible for significant load transmission and redistribution, leading to considerable stress concentration at their connections with the platform. These connection regions often feature geometric discontinuities, preventing gradual stress transfer and resulting in localized stress concentrations.

Fig. 23(b) presents the stress distribution and deformation response of the blade and its internal shear webs. During operation, the blade undergoes large flapwise deformation due to aerodynamic loading, with maximum deflection occurring at the blade tip. To better visualize the deformation characteristics, the flapwise deformation is magnified by a factor of 3. Compared to the tower and platform, the blade primarily sustains aerodynamic loads, and thus exhibit a relatively low overall stress level. The main spar, serving as the structural backbone of the blade, withstands bending stresses arising from aerodynamic moments and centrifugal forces. As a result, the material regions near the main spar, especially at the connections with the shear webs, exhibit significantly elevated stress. The enlarged detail views show that peak stress concentrations occur in the blade root transition region, mainly due to stiffness gradients resulting from laminate overlaps and manufacturing discontinuities. These gradients also lead to shear stress concentrations in the shear web at the blade root. The maximum stresses in the blade and shear web at the root are 1.14×10^7 Pa and 6.42×10^7 Pa, respectively. In contrast, stress at the blade tip is minimal. Therefore, in future laminate design optimization, particular focus should be placed on mitigating fatigue damage in the blade root transition zone.

5.3.2. Aero-elastic response of blade

Under sustained aerodynamic loading, the FOWT blades undergo elastic bending, with the flapwise direction, which is generally aligned with the inflow, exhibiting the most pronounced deformation. Fig. 24 presents the deformation response of a single blade at various spanwise positions. As shown in Fig. 24(a) (where the background color indicates rotor rotation cycles), the blade deformation fluctuates periodically throughout each rotation. The tower shadow effect induces localized small-amplitude disturbances in the response curves. With increasing spanwise distance, the blade deformation and vibration amplitude show a nonlinear growth trend. This is primarily due to the significant elastic deformation near the blade tip, which alters the local inflow conditions. In addition, the 6-DOF motions of the FOWT platform further intensify the unsteady aerodynamic disturbances, leading to highly unstable deformation amplitudes. During the total response time, the maximum displacement of the blade tip in the flapwise direction reaches 3.71 m. Fig. 24(b) illustrates the average flapwise deformation along the blade span. It can be observed that deformation near the blade root ($x/L \leq 0.2$) is negligible, with an average value of only 0.043 m, whereas the blade tip exhibits a much larger average deformation of up to 3.18 m. This non-uniform deformation pattern highlights the structural vulnerability of the blade tip region. Therefore, optimizing material distribution and laminate design of the blade is essential to enhance the resistance to unsteady loading.

Fig. 25 presents the complex aeroelastic response of the FOWT blade under multi-physics coupling effects. Influenced by nonlinear deformation and the 6-DOF motions of the platform, the local angle of attack of the FOWT blade changes, resulting in a redistribution of circulation in the surrounding flow field. The local flow around the airfoil transitions from attached to separated, as shown in Fig. 25(a), which triggers strong vortex shedding and even dynamic stall, resulting in a notable reduction in aerodynamic performance. On the right side of Fig. 25(a), the vorticity contours at the hub position downstream of the rotor are shown for both the BFWT and FOWT. It is seen that a large-scale vortex shedding phenomenon behind the blade trailing edge of the FOWT blades, along with additional vortex rings forming within the rotor area, indicating an enhanced unsteady effect in the flow field. By contrast, the BFWT shows vortex shedding only near the blade root and tip regions,

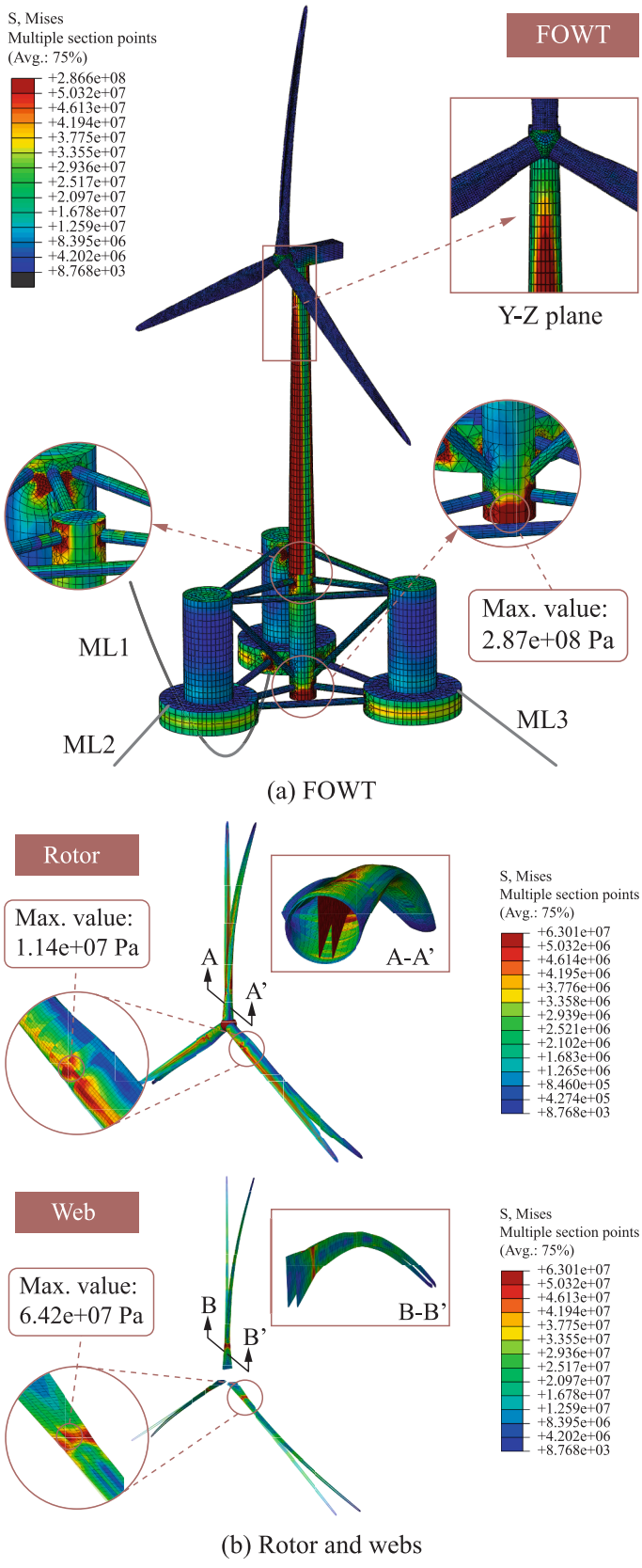

Fig. 23. Structural stress and deformation of the FOWT.

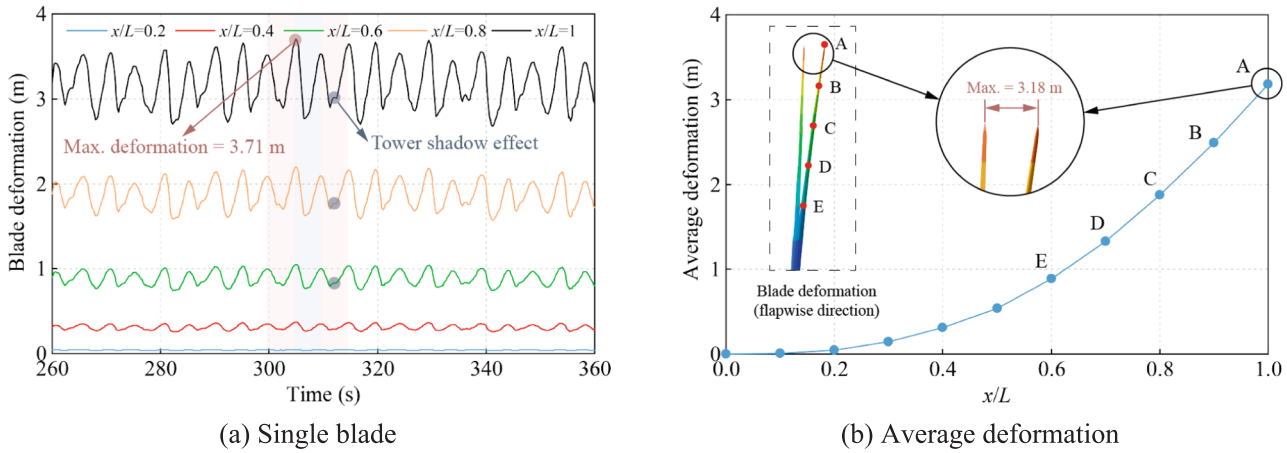

Fig. 24. Flapwise deformation of FOWT blade.

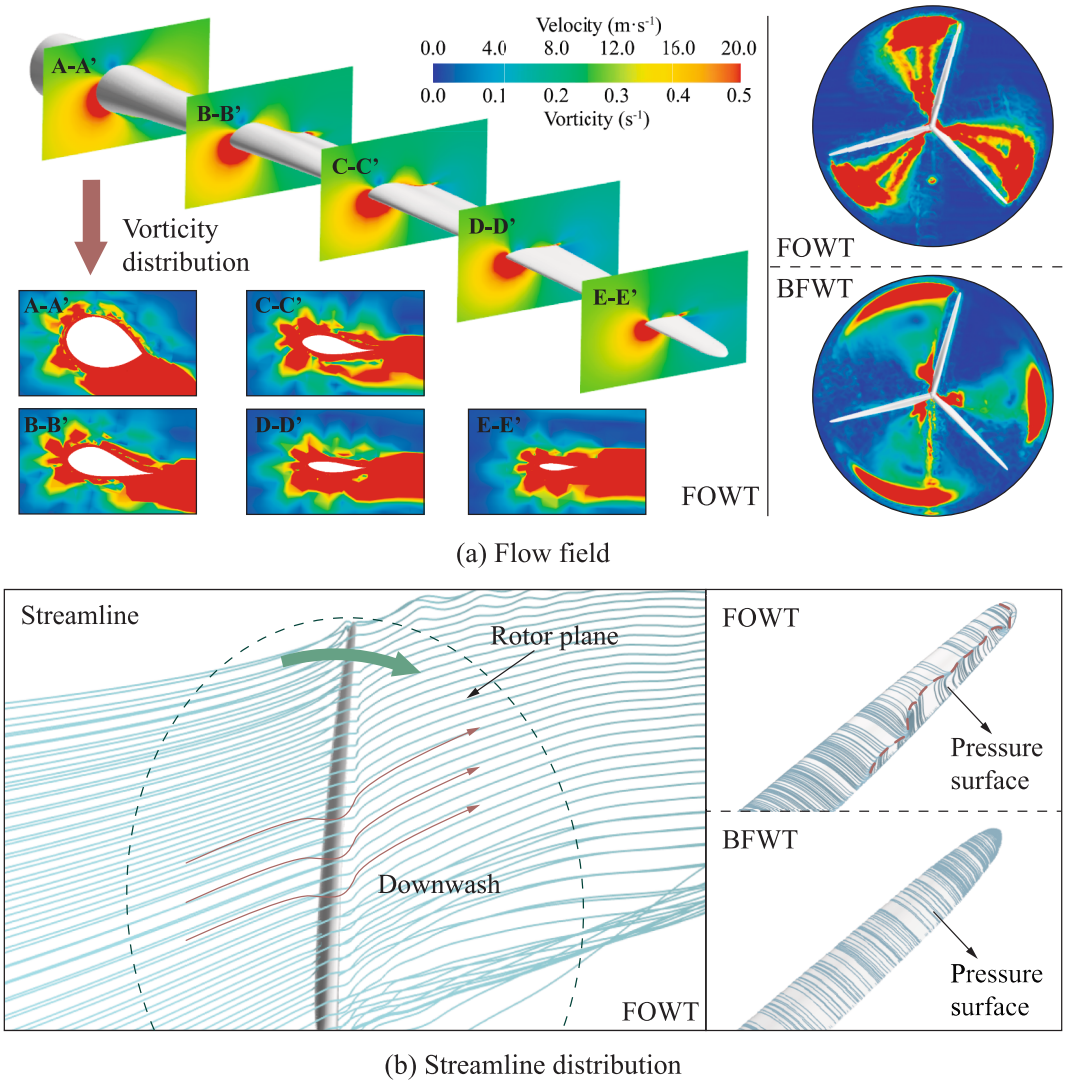

Fig. 25. Velocity field and streamline distribution on the blade surface.

with more stable vortex development.

Fig. 25(b) shows the streamline distribution around the FOWT blade and along its pressure side. Due to circulation, a velocity component perpendicular to the incoming flow is induced on the airfoil surface, generating a downwash effect as the airflow passes over the blade. Near the blade root, where the airfoil is typically thicker and less aerodynamically efficient, the downwash effect is relatively weak. However, from the mid-span to the tip region, where aerodynamic performance

and induced velocity are greater, the downwash angle increases accordingly. Because the induced velocity also has a tangential component, the downwash flow propagates in a helical pattern. The figure shows that, due to elastic deformation and platform motion, the downwash flow behind the blade tip exhibits considerable fluctuations. In addition, large variations in the angle of attack produce a strong adverse pressure gradient near the trailing edge on the pressure side, causing boundary layer separation and the formation of a free shear layer. As a result, the streamlines over the pressure surface become unstable and curl into vortex structures.

5.3.3. *Contact effect between mooring and seabed*

There exists a complex frictional contact interaction between the mooring system and the seabed. While this contact reduces the amplitude of mooring tension responses to some extent, the resulting non-uniform tension distribution tends to promote fatigue accumulation. Moreover, stress concentrations at the contact interface can lead to localized wear of the mooring lines, especially during repeated separation and recontact cycles with the seabed caused by platform motion. These effects intensify the nonlinear dynamic response of the mooring system, increase the risk of structural fatigue and failure, and thus pose a serious threat to the safe and stable operation of the FOWT. Therefore, understanding the contact behavior between the moorings and the seabed is of critical importance.

Fig. 26 presents the contact opening distance and seabed pressure distribution for each FOWT mooring. Due to its alignment with the wind-wave loading direction, ML2 is more prone to periodic seabed separation and recontact, and has a shorter touchdown length compared to ML1 and ML3. This behavior not only amplifies the nonlinearity of the tension response but also increases the risk of fatigue damage and localized abrasion. When the FOWT moves in the + X direction, the suspended segment length of ML2 increases, while the contact pressure in the touchdown zone decreases gradually. During this stage, the tension in ML2 gradually increases until it reaches equilibrium with the inertial force of the FOWT at the surge balance point. When the FOWT moves in the −X direction, the suspended segment of ML2 shortens accordingly, and the seabed contact pressure in the touchdown zone gradually increases, reaching its maximum before the onset of the next fluctuation cycle. It is also worth noting that the seabed contact pressure of ML1 and ML3 remains relatively high throughout. Influenced by the sway motion, ML3 experiences slightly higher contact pressure than ML1, with a maximum value reaching 147.6 Pa.

Fig. 27 shows the variation trends of the contact opening distances for selected beam elements of MLs, located approximately one-third of the way from the anchor point along each ML. The results indicate that the reciprocating surge motion of the FOWT in the + X direction significantly increases both the opening distance and fluctuation amplitude of Element 2. Its variation trend closely aligns with that of the surge response shown in Fig. 21(e). After 120 s, the average opening distance of Element 2 reaches 14.08 m, with an average fluctuation amplitude of 9.47 m. During this phase, ML1 and ML3 remain in a relatively relaxed state, resulting in smaller opening distances and lower fluctuation amplitudes for Elements 1 and 3.

Although ML1 and ML3 are symmetrically distributed with respect to the X-axis, the FOWT exhibits sway motion biased toward the + Y direction, which is aligned with the anchor direction of ML3. As a result, the opening distance of Element 3 further decreases. These findings help to improve the understanding of mooring dynamics under complex sea states and provide theoretical guidance for the optimal design of FOWT mooring systems.

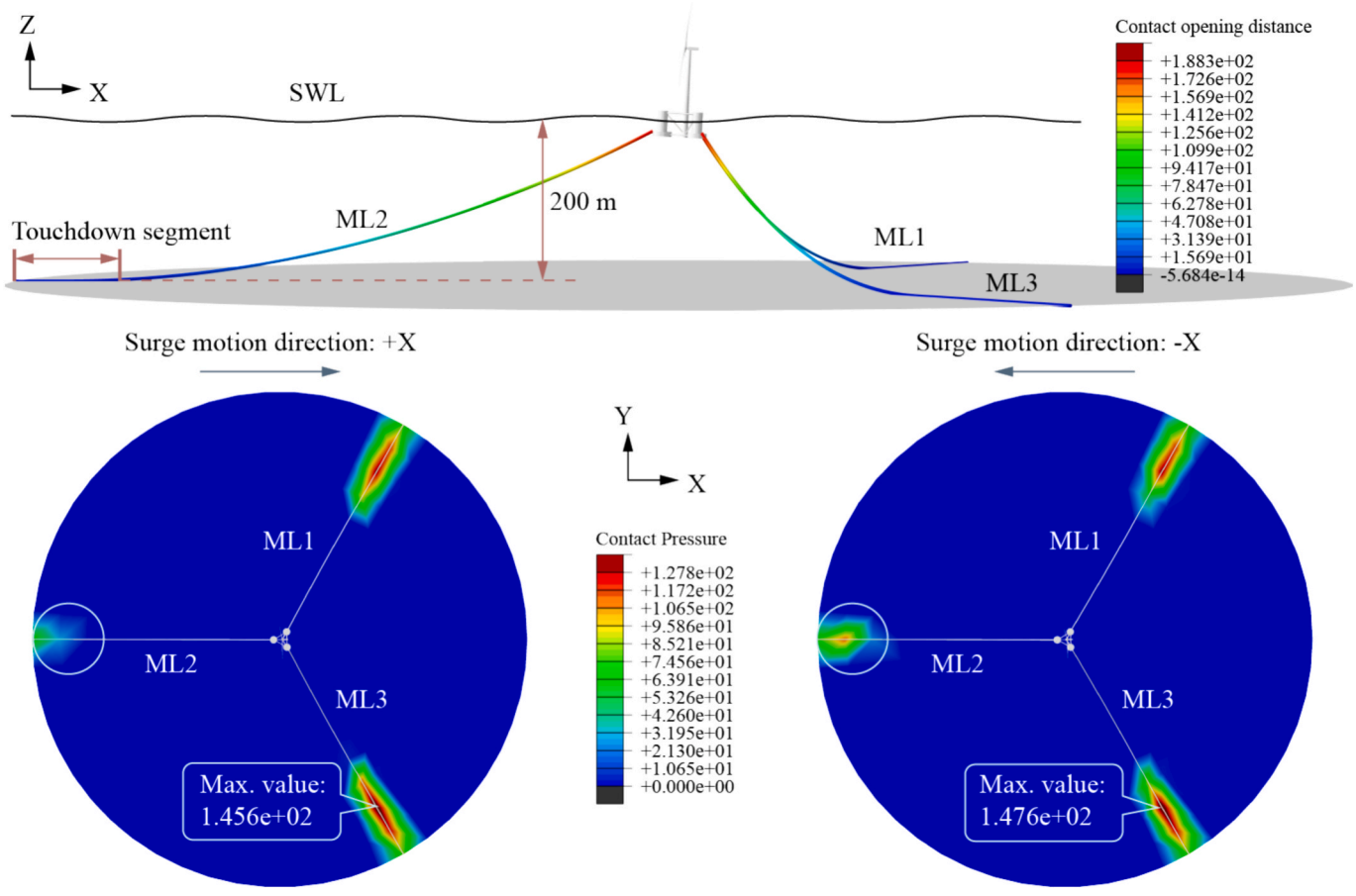

Fig. 26. Opening distance and contact pressure between ML and the seabed.

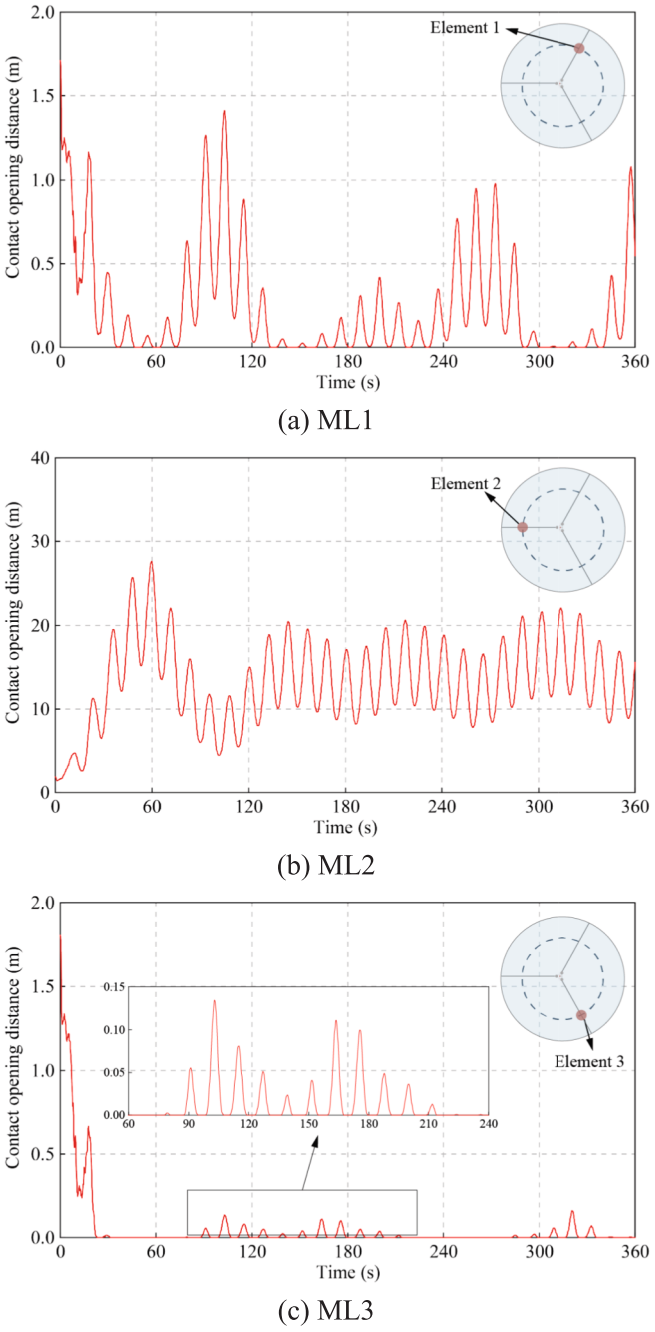

Fig. 27. Variation trend of the ML contact opening distance.

5.4. *Applicability assessment of the CFD-FEM framework*

The proposed multi-physics modeling approach enables in-depth analysis of nonlinear aero-hydro-structural coupling in FOWTs, which is challenging for mid-fidelity tools (e.g., FAST with HydroDyn and ElastoDyn) due to the simplified assumption models [58]. For example, HydroDyn uses PFT for platform-wave interaction, which cannot capture large-amplitude nonlinear motions under complex wind-wave conditions. ElastoDyn typically employs simplified beam elements for blade stiffness and mass, neglecting high frequency vibrations and aeroelastic effects. Furthermore, ElastoDyn usually relies on steady or quasi-steady aerodynamic models (BEMT) that cannot capture transient aerodynamic phenomena.

In contrast, the CFD-FEM approach solves unsteady flow (e.g., dynamic stall, large vortex structures), platform motion, wake interactions, and blade bending-torsion coupling with aeroelastic effects. Its main limitation is high computational cost, which restricts its application in cases requiring a large number of operating conditions or long-duration analysis. Therefore, in practical engineering, both mid-fidelity and high-fidelity methods have their own domain of application. They should be used in parallel to balance computational efficiency and accuracy, thereby meeting the requirements at different stages of the engineering process.

The applicability of the proposed CFD-FEM method is as follows:

- key design stage optimization and verification

Supports preliminary optimization of blade aerodynamic, platform structure, mooring system, and layout through accurate multi-physics coupling. In detailed optimization, it can identify potential design issues early, avoiding major large-scale modifications, reducing costs, and improving efficiency.

- Safety assessment under complex or extreme conditions

Under challenging climatic conditions, traditional mid-fidelity models often fail to accurately predict FOWT dynamic response and risks. The CFD-FEM method can capture strong nonlinear, transient effects, and complex FSI phenomena, providing a more realistic basis for structural safety and reliability assessments.

6. Conclusions

In this study, a high-fidelity coupled model of the FOWT is developed using the CFD-FEM method to accurately solve its aero-elastic-hydro-mooring dynamics. The numerical simulation of the fully coupled FOWT is conducted under wind and wave loading. The aerodynamic performance of the rotor and the fluctuations of blade torque are analyzed systematically. The coupling mechanisms of the 6-DOF motions of the platform are elucidated. Additionally, the structural dynamics of the entire FOWT system, the aeroelastic responses of the blades, and the frictional contact effects between the mooring system and the seabed are revealed. The main conclusions are:

(1) Due to the influence of 6-DOF motions, the dynamic inflow conditions of the FOWT rotor exhibit continuous variation, leading to significantly greater fluctuations in aerodynamic power and thrust compared to BFWTs. The presence of low-order high-frequency vibrations further alters the local angle of attack on the FOWT blades, causing additional minor local fluctuations in the power output and thrust response curves. These nonlinear disturbances are further amplified by dynamic interactions among the various subsystems, resulting in reductions of 6.84 % and 3.50 % in the average power and thrust of the FOWT, respectively, compared to those of the BFWT.

(2) The wake of the FOWT exhibits more intense shear layer disturbances and vortex interactions. The generated vortex rings form a denser vortex structure in the near wake region, significantly enhancing the turbulence intensity and the wake dissipation rate. High-frequency dynamic variations in the angle of attack induce spanwise multipoint flow separation on the blades, leading to continuous vortex shedding zones. Additionally, the free-surface fluctuations induced by wave action alter the vertical velocity gradient of the nearby fluid, accelerating the transition of the wake into the turbulent mixing stage. In contrast, the BFWT wake maintains a more stable low-velocity core and coherent shear layer structure, resulting in slower dissipation and a longer recovery distance.

(3) Under wind and wave loading, the FOWT undergoes reciprocating surge, heave, and pitch motions synchronized with the wave excitation periods. Second-order wave forces induce platform drift, causing variations in mooring restoring force and moment. These variations lead to dynamic equilibrium positions for surge, heave, and pitch at 6.98 m, −0.29 m, and 4.07 deg, respectively. The sway and roll

responses of the FOWT are less sensitive to wave excitation due to the directionality of wave incidence. However, during the platform drift motion, the changes in platform attitude and the redistribution of rotor thrust, both caused by roll, resulted in an increase of the yaw amplitude and a longer time to reach the steady state.. Furthermore, the tension response of mooring line ML2 is directly affected by the surge motion of the platform, with tension fluctuations remaining at a consistently high amplitude.

(4) The aerodynamic thrust from the rotor significantly increases stress on the windward and leeward sides of the tower, with the maximum stress occurring at the tower base. Due to the concentrated mass loads from the tower, nacelle, and rotor, the base of the platform's main column experiences the highest stress in the entire FOWT system, which reaches 2.87×10^8 Pa. The cross and diagonal braces primarily function in load transmission and conversion, leading to localized stress concentrations at their connections with the platform. Compared to the platform and tower, the overall stress level in the blades is lower. As the main load-bearing structure, the blade main spar exhibits significantly increased stress at the junction with the webs. Additionally, the blade root transition section is prone to stress concentration due to stiffness gradients caused by ply overlaps and manufacturing discontinuities.

(5) Under aerodynamic loading, the FOWT blade undergoes significant flapwise deformation, which increases nonlinearly from the blade root to the tip. Influenced by both the elastic deformation and platform 6-DOF motion, the angle of attack from the mid-span to the tip varies considerably, leading to flow separation and even dynamic stall on the local airfoil surfaces. Due to strong aerodynamic forces and high induced velocities, the downwash angles at the mid and tip sections are larger and exhibit greater fluctuations. Moreover, a strong adverse pressure gradient develops near the trailing edge on the pressure side of the blade tip, inducing boundary layer separation, which causes the streamlines along the pressure surface to become unstable and curl up.

(6) Influenced by the surge motion of the platform, ML2 is more prone to separate from, and recontact, the seabed periodically, resulting in intensified nonlinear fluctuations in tension with consistently high amplitudes. Compared to ML2, ML1 and ML3 have longer touchdown lengths, and therefore experience significantly greater contact pressure with the seabed. Due to the −Y direction sway motion, the contact pressure of ML3 is higher than that of ML1, with a peak value reaching 147.6 Pa. The contact opening distances between beam elements near the seabed in the MLs indicate that the variation trend of the opening distance in ML2 closely corresponds to the platform surge motion, while the opening distances and amplitudes in ML1 and ML3 remain relatively small, indicating a slack state.

In summary, the proposed CFD-FEM approach can provide reliable technical guidance for the optimization and validation of FOWTs during the critical design phases, as well as for safety assessments under specific complex/extreme operating conditions.

7. Future works

Based on the fully coupled simulation results of this study, future research on the aerodynamic design and load management of FOWTs could consider the following aspects:

- Blade pre-bend and twist design, and composite laminate optimization

The coupling of platform motion and blade bending and twisting leads to significant variations in the wind inflow conditions. Future research could incorporate pre-bend and twist designs in the blade to help maintain a consistent angle of attack, thereby reducing aerodynamic efficiency losses. Additionally, the blade root experiences high stress concentrations, which could be addressed by optimizing composite laminate design to enhance structural strength and improve the overall durability of the blade.

- Platform structural design and mooring system optimization

The 6-DOF motion of the platform has a significant impact on the aerodynamic performance of the FOWT and mooring tension responses. Existing platform improvement solutions often adopt mature or widely used geometries, which may lead to homogenized platform designs that overlook the unique structural characteristics. Future studies could draw inspiration from fluid dynamics in nature to explore innovative platform designs. Given the periodic contact between the mooring lines and seabed, as well as the significant increases in the mooring tension on the windward wave side, it is recommended to use more fatigue-resistant materials and optimize the mooring layout.

- Performance evaluation of large-scale floating horizontal/vertical axis wind turbines

The proposed FSI framework has no scalability limitations in theory and coupling approach. With appropriate mesh resolution and time step adjustment, it can be applied to the aero-elastic-hydro-mooring dynamics simulation of large-scale floating horizontal/vertical axis wind turbines. Although larger wind turbines require higher computational resources, this challenge can be addressed through the overset grid interface optimization and parallel computing.

CRediT authorship contribution statement

Haoda Huang: Writing – original draft, Visualization, Validation, Software, Investigation, Formal analysis, Data curation. **Qingsong Liu:** Writing – review & editing, Supervision, Resources, Methodology, Investigation. **Gregorio Iglesias:** Writing – review & editing, Validation, Supervision, Resources, Methodology. **Chun Li:** Writing – review & editing, Supervision, Project administration, Funding acquisition.

Declaration of competing interest

The authors declare that they have no known competing financial interests or personal relationships that could have appeared to influence the work reported in this paper.

Acknowledgements

The authors would like to acknowledge the support of National Key R&D Program of China (No. 2024YFA1012500) and National Natural Science Foundation of China (Grand No. 52376204). The numerical simulations were performed on the Barkla HPC at the University of Liverpool, whose support is gratefully acknowledged.

Data availability

The CFD and FEM datasets, including fully coupled flow field visualizations and structural stress–strain results generated during the current study, are available in the Github repository [DOI: https://github.com/hhdusst0217/The-post-processed-flow-field-results-of-the-two-way-FSI-simulation-for-FOWTs.git].

References

[1] Xie Z, Lin Z, Cai Q, et al. Aerodynamic reconstruction of wind turbines using terrestrial laser scanning: Methodology, validation, and error analysis. Energ Conver Manage 2025;334:119792.
[2] Wei Z, Borthwick A, Cao F, et al. Power performance of an offshore floating hybrid wind and wave energy converter. Energ Conver Manage 2025;341:120023.
[3] Zhu K, Shi HD, Zheng SM, et al. Hydrodynamic analysis of hybrid system with wind turbine and wave energy converter. Appl Energy 2023;350:121745.
[4] Council GWE. Global wind report 2025. Lisbon: GWEC; 2025.
[5] Pivert FL, Roberts A, López-Santander A, et al. Data driven multi-objective optimization of the scheduling for towing a floating offshore wind turbine between

assembly port and installation location throughout a year. Appl Ocean Res 2025;157:104492.
[6] Chirosca AM, Rusu L, Bleoju A. Study on wind farms in the North Sea area[J]. Energy Rep 2022;8:162–8.
[7] Edwards EC, Holcombe A, Brown S, et al. Trends in floating offshore wind platforms: A review of early-stage devices. Renew Sustain Energy Rev 2024;193:114271.
[8] Qiao DS, Zhou YC, Xu BB, et al. Dynamic response analysis of a fully coupled aerodynamic-hydrodynamic-mooring-anchor floating offshore wind turbine. Ocean Eng 2024;312:119085.
[9] Yang L, Liao KP, Ma QW, et al. Coupled aero-servo-elastic method for floating offshore wind turbine wake analysis. Ocean Eng 2024;307:118108.
[10] Zhu YP, Zhong J, Zhu YF, et al. Effects of the yaw error and the fault conditions on the dynamic characteristics of the 15 MW offshore semi-submersible wind turbine. Ocean Eng 2024;300:117440.
[11] Xiao Y, Wang XB, Sun XY, et al. Load reduction and mechanism analysis of cyclic pitch regulation on wind turbine blades under yaw conditions. Ocean Eng 2025;321:120361.
[12] Cao JF, Qin ZJ, Ju Y, et al. Study of air compressibility effects on the aerodynamic performance of the IEA-15 MW offshore wind turbine. Energ Conver Manage 2023;282:116883.
[13] Hayat K, Gorostidi A, Donazar Moriones C, et al. Flutter performance of bend-twist coupled large-scale wind turbine blades. J Sound Vib 2016;370:149–62.
[14] Yang L, Li BB, Dong YH, et al. Large-amplitude rotation of floating offshore wind turbines: A comprehensive review of causes, consequences, and solutions. Renew Sustain Energy Rev 2025;211:115295.
[15] Haider R, Shi W, Lin ZB, et al. Coupled analysis of floating offshore wind turbines with new mooring systems by CFD method. Ocean Eng 2024;312:119054.
[16] Ma G, Liu LH, Wang HW, et al. Reconstruction of scaled FOWT blades for achieving aerodynamic similarity with control strategy adjustment. Ocean Eng 2025;317:120078.
[17] Zhao ZX, Chang S, Li X, et al. Experimental study on dynamic responses of a new semi-submersible supporting platform concept for 10 MW wind turbines. Ocean Eng 2025;318:120168.
[18] Kim Y, Madsen HA, Aparicio-Sanchez M, et al. Assessment of blade element momentum codes under varying turbulence levels by comparing with blade resolved computational fluid dynamics. Renew Energy 2020;160:788–802.
[19] Wang SZ, Chuang WL. Dynamic analysis of breaking wave impact on a floating offshore wind turbine via smoothed particle hydrodynamics. Mar Struct 2025;100:103731.
[20] Yang Y, Bashir M, Michailides C, et al. Development and application of an aero-hydro-servo-elastic coupling framework for analysis of floating offshore wind turbines. Renew Energy 2020;161:606–25.
[21] Yang HS, Tongphong W, Ali A, et al. Comparison of different fidelity hydrodynamic-aerodynamic coupled simulation code on the 10 MW semi-submersible type floating offshore wind turbine. Ocean Eng 2023;281:114736.
[22] Xie SY, Zhang CL, Kan YZ, et al. Aero-hydro-servo-elastic coupled modeling and dynamics analysis of a four-rotor floating offshore wind turbine. Ocean Eng 2023;272:113724.
[23] Tang RJ, Huang W, Li XY, et al. Investigation of the dynamic response of Floating Offshore Wind Turbines based on vortex lattice aerodynamic model. Eng Anal Bound Elem 2025;177:106243.
[24] Wang TY, Zhu K, Cao FF, et al. A coupling framework between OpenFAST and WEC-Sim. Part I: Validation and dynamic response analysis of IEA-15-MW-UMaine FOWT. Renew Energy 2024;225:120249.
[25] Lamei A, Hayatdavoodi M, Riggs HR, et al. Wave-current-wind interaction with elastic floating offshore wind turbines. Eng Anal Bound Elem 2025;171:106052.
[26] Wang K, Zhao MS, Tang QH, et al. Investigating effects of pitch motions on aerodynamics and wake characteristics of a floating offshore wind turbine. Energ Conver Manage 2025;326:119402.
[27] Zhang WZ, Calderon-Sanchez J, Duque D, et al. Computational fluid dynamics (CFD) applications in floating offshore wind turbine (FOWT) dynamics: a review. Appl Ocean Res 2024;150:104075.
[28] Sun QH, Li G, Duan L, et al. The coupling of tower-shadow effect and surge motion intensifies aerodynamic load variability in downwind floating offshore wind turbines. Energy 2023;282:128788.
[29] Guo YZ, Wang XD, Mei YH, et al. Effect of coupled platform pitch-surge motions on the aerodynamic characters of a horizontal floating offshore wind turbine. Renew Energy 2022;196:278–97.
[30] Cai YF, Li X, Leng SD, et al. Effect of combined surge and pitch motion on the aerodynamic performance of floating offshore wind turbine. Ocean Eng 2024;306:118061.
[31] Arabgolarcheh A, Benini E, Anbarsooz M. Development of an actuator line model for simulation of floating offshore wind turbines. Proceedings of the ASME 2021 Power Conference. 2021.
[32] Arabgolarcheh A, Micallef D, Rezaeiha A, et al. Modelling of two tandem floating offshore wind turbines using an actuator line model. Renew Energy 2023;216:119067.
[33] Zhou Y, Xiao Q, Peyrard C, et al. Assessing focused wave applicability on a coupled aero-hydro-mooring FOWT system using CFD approach. Ocean Eng 2021;240:109987.
[34] Zhou Y, Xiao Q, Liu YC, et al. Exploring inflow wind condition on floating offshore wind turbine aerodynamic characterisation and platform motion prediction using blade resolved CFD simulation. Renew Energy 2022;182:1060–79.
[35] Alkhabbaz A, Hamza H, Daabo AM, et al. The aero-hydrodynamic interference impact on the NREL 5-MW floating wind turbine experiencing surge motion. Ocean Eng 2024;295:116970.
[36] Sebastian T, Lackner MA. Development of a free vortex wake method code for offshore floating wind turbines. Renew Energy 2012;46:269–75.
[37] Sebastian T, Lackner M. A Comparison of First-Order Aerodynamic Analysis Methods for Floating Wind Turbines//48th AIAA Aerospace Sciences Meeting Including the New Horizons Forum and Aerospace Exposition. America: AIAA; 2010.
[38] Arabgolarcheh A, Rouhollahi A, Benini E. Analysis of middle-to-far wake behind floating offshore wind turbines in the presence of multiple platform motions. Renew Energy 2023;208:546–60.
[39] Mian HH, Machot FA, Ullah H, et al. Advances in computational intelligence for floating offshore wind turbines aerodynamics: Current state review and future potential. Renew Sustain Energy Rev 2025;224:116098.
[40] Huang B, Luo WL, Ren QY, et al. Random wave forces on the submerged box girder superstructure of coastal bridges based on potential flow theory. Ocean Eng 2022;248:110739.
[41] Zhang Y, Stansby P, Li GQ. A study of nonlinear hydrodynamic and mooring modelling for the Volturn floating wind platform in comparison with experiments. Appl Ocean Res 2025;158:104550.
[42] Kim T, Hansen AM, Branner K. Development of an anisotropic beam finite element for composite wind turbine blades in multibody system. Renew Energy 2013;59:172–83.
[43] Jonkman JM, Butterfield S, Musial W, et al. Definition of a 5-MW Reference Wind Turbine for Offshore System Development. America: Office of Scientific & Technical Information Technical Reports; 2009.
[44] Robertson A, Jonkman J, Masciola M, et al. Definition of the Semisubmersible Floating System for Phase II of OC4. America: USDOE Office of Energy Efficiency and Renewable Energy Wind Power Technologies Office. 2014.
[45] Resor BR. Definition of a 5mw/61.5m wind turbine blade reference model. New Mexico: Sandia National Laboratories 2013.
[46] Zouheyr D, Lotf B, Abdelmadjid B. Improved hardware implementation of a TSR based MPPT algorithm for a low cost connected wind turbine emulator under unbalanced wind speeds. Energy 2021;232:121039.
[47] Zhang P, Zhang H, Luo T, et al. Dynamic thrust and power measurement for a scaled floating wind turbine in wind tunnel. Energ Conver Manage 2024;322:119188.
[48] Wang Q, Hu J, Yang S, et al. Towards machine learning applications for structural load and power assessment of wind turbine: An engineering perspective. Energ Conver Manage 2025;324:119275.
[49] Meng H, Su H, Guo J, et al. Experimental investigation on the power and thrust characteristics of a wind turbine model subjected to surge and sway motions. Renew Energy 2022;181:1325–37.
[50] Nugraha AD, Garingging RA, Wiranata A, et al. Comparison of “Rose, Aeroleaf, and Tulip” vertical axis wind turbines (VAWTs) and their characteristics for alternative electricity generation in urban and rural areas. Results Eng 2025;25:103885.
[51] Jeong K, Kim S. Structural response of submerged floating tunnels with free-end boundary condition based on an analytical approach. Appl Ocean Res 2024;143:103861.
[52] Jiao J, Chen Z, Xu W, et al. Asymmetric water entry of a wedged grillage structure investigated by CFD-FEM co-simulation. Ocean Eng 2024;302:117612.
[53] Garoosi F, Kantzas A, Irani M. Numerical simulation of wave interaction with porous structure using the coupled Volume-Of-Fluid (VOF) and Darcy-Brinkman-Forchheimer model. Eng Anal Bound Elem 2024;166:105866.
[54] Zhang L, Lin S, Wang C, et al. A direct analysis approach for ejection problem of the independent escape capsule. Ocean Eng 2017;145:95–111.
[55] Cheng P, Huang Y, Wan D. A numerical model for fully coupled aero-hydrodynamic analysis of floating offshore wind turbine. Ocean Eng 2019;173:183–96.
[56] Tran TT, Kim DH. Fully coupled aero-hydrodynamic analysis of a semi-submersible FOWT using a dynamic fluid body interaction approach. Renew Energy 2016;92:244–61.
[57] Deng Z, Xiao Q, Huang Y, et al. A general FSI framework for an effective stress analysis on composite wind turbine blades. Ocean Eng 2024;291:116412.
[58] Gao Y, Chen Y, Wang L. Development of an aero-elastic-servo-hydro-mooring coupling framework for FOWT system. Appl Ocean Res 2025;161:104676.